

RESEARCH

Open Access



Modelling of flow through naturally fractured geothermal reservoirs, Taupō Volcanic Zone, New Zealand

Warwick M. Kissling^{1*} and Cécile Massiot¹

*Correspondence:
w.kissling@gns.cri.nz

¹ GNS Science, 1 Fairway Drive,
Avalon, PO Box 30368, Lower
Hutt 5040, New Zealand

Abstract

Background: Numerous fractures are observed in fractured geothermal reservoirs on borehole images in the Taupō Volcanic Zone (TVZ), Aotearoa New Zealand. These fractures are necessary to explain the sustained reservoir permeabilities despite the low matrix porosity. However, conventional continuum models do not adequately represent fluid flow through these fractured rocks.

Methods: We present new Discrete Fracture Network (DFN) codes that model fractures and associated fluid flow in 2-D at reservoir scales to represent typical rock types found in TVZ reservoirs. Input parameters are derived from interpretations of borehole images at the Rotokawa and Wairakei geothermal fields where fractures have high dip magnitudes ($> 60\text{--}70^\circ$). This paper focuses on the effect of fracture density along virtual boreholes (P_{10}), that is in average 0.6 m^{-1} in sheet-like andesites; 0.8 m^{-1} in ignimbrites and 1.7 m^{-1} in rhyolite lavas.

Results: The number of fractures in the models scale linearly with the input P_{10} in virtual boreholes. The percolation threshold, where the backbone of fractures is connected across the entire model domain, is reached for $P_{10} > 0.24\text{ m}^{-1}$. Above this threshold, mean flow measured along the mean fracture direction scales linearly with P_{10} . For $P_{10} > 0.4\text{ m}^{-1}$ the permeability anisotropy lies in the interval 13 ± 3 , with the scatter decreasing as P_{10} increases. The pressure distributions in individual DFN realisations are highly variable, but averages of 50 realisations converge towards those given by equivalent continuum models. Probability density functions resulting from DFN realisations can therefore be used to constrain continuum models. Tracing of fluid particles through the DFN shows that particles can take numerous pathways to define a swath of paths. The travel time of particles over 1 km follows a distribution similar to real tracer tests, with arrivals peaking at 1–2 days and a long tail stretching to over 200 days.

Conclusions: The new codes, calibrated to real measurements of fracture geometries in borehole images of the TVZ, reproduce patterns of flows in fractured geothermal systems. Mean flows and permeability anisotropies derived from the DFNs can be used to improve modelling of flows through fractured geothermal reservoirs using continuum models at a limited computational cost.

Keypoints

- New fracture modeling codes and with input from fracture measurements in geothermal boreholes.
- Probability density functions of mean flows and flow anisotropy through fractured networks at reservoir scale for rock types found in TVZ geothermal reservoirs.
- Calibration for continuum models.
- Quantification of fluid dispersion: implications for tracer test interpretation.

Keywords: Fractured reservoirs, Discrete fracture network, Permeability, Anisotropy, New Zealand

Plain Language Abstract

Rocks in New Zealand geothermal systems are highly fractured. Hot water flows through networks of these fractures and is collected in boreholes to generate electricity. It is important for the geothermal industry to understand how hot water flows through fractured rock so that expensive boreholes can be optimally located and energy generation maximized. Rocks in New Zealand geothermal systems are highly fractured. Hot water flows through networks of these fractures and is collected in boreholes to generate electricity. In this paper we use data collected from boreholes in two New Zealand geothermal fields to study how easily hot water flows through the main types of volcanic rocks commonly found in these fields. The observations made in boreholes tell us how many fractures cross the borehole, how big they are, and in what direction they lie. We have developed computer programs that extrapolate these measurements in a realistic way from close to the borehole to the whole geothermal reservoir, and then to calculate the flows through the resulting fracture networks. Because these networks can be so irregular, we calculate thousands of different examples to understand the likely variability of the flows through them. Averages of many fracture models, at least 50, give similar results to traditional models used by the geothermal industry, which don't consider fractures. This tells us that the traditional models are missing a lot of important details. Results from our fracture models can therefore be used in traditional models to improve the way they consider flows in fractured geothermal reservoir.

Introduction

The most productive geothermal boreholes are observed in volcanic or volcanoclastic systems with well-developed, permeable fracture networks (Davatzes and Hickman 2010; Sepulveda et al. 2012; Jolie et al. 2016, 2021; McNamara et al. 2016; Bolos et al. 2019; Intani et al. 2020; Liotta et al. 2021). Natural fracture networks can support economic use of geothermal systems even where reservoir formations have low matrix permeability (less than 10^{-16} m²) (Siratovich et al. 2014) and are common in the Taupō Volcanic Zone (TVZ), Aotearoa New Zealand. A major challenge for obtaining productive boreholes in fractured geothermal reservoirs is locating fluid-bearing permeable structures with sustainable recharge, in 3-D and on reservoir scales of ~1 km. Major flow paths are often provided by large faults and their damage zones that can be modelled deterministically (Dezayes et al. 2010; Faulkner et al. 2010; Ramadhan and Masri 2014; Vidal and Genter 2018; McNamara et al. 2019). Pervasive networks of smaller fractures that can connect at reservoir scale between large faults also need to be considered

to understand reservoir permeability, heat losses to the matrix, and to interpret tracer tests (Grant and Bixley 2011; Winick et al. 2015).

In fractured geothermal reservoirs, borehole images are increasingly used to map the numerous small fractures that cannot be resolved by geophysical imaging or stratigraphic offsets between nearby boreholes. Borehole images allow to quantify fractures' geometric parameters (orientation, density along the borehole, apparent thickness) and in-situ stress (Barton and Zoback 1992; Genter et al. 1997; Davatzes and Hickman 2010; Halwa et al. 2013; McNamara et al. 2015, 2019; Massiot et al. 2017a). The numerous fractures observed along borehole images between reservoir-scale faults may arise from the primary rock type (e.g. cooling joints in lavas and ignimbrites, joints in sedimentary rocks, old fractures in metamorphic rocks) (Massiot et al. 2017a), be formed under the current in-situ stress field but not clearly linked to the damage zone of a specific fault (Stimac et al. 2019) or inherited from previous tectonic events (Sieh and Natawidjaja 2000; Glaas et al. 2021). Some permeable zones coincide with fractures observed in borehole images that cannot be directly linked to a mapped fault (Ramadhan and Masri 2014; McNamara et al. 2015, 2019; Baujard et al. 2017; Massiot et al. 2017b; Norini et al. 2019; Intani et al. 2020).

Continuum heat and fluid transport codes such as TOUGH2 are commonly used to model fluid and heat flow through geothermal systems (Pruess 1991), but this approach is not satisfactory when the reservoir permeability is dominated by fractures. Indeed, in continuum models, permeability and other rock properties are ascribed to computational grid blocks of size on the order of 10–100 m (e.g. Pruess 1991). In fractured reservoirs, fluid flow is confined to much smaller 'fracture aperture' length scales (< 1 m) while still extending over reservoir scales (Bonnet et al. 2001). The MINC approach in TOUGH2 considers fractures in continuum models with modest computational cost but is unable to represent real fracture systems (Pruess 1992). Representing pervasive fracture networks in a reservoir-scale continuum modelling is computationally expensive, impractical for day-to-day field management, and prone to large uncertainties due to incomplete knowledge of the reservoir-wide fracture system.

Discrete Fracture Network (DFN) models are stochastic realisations of fracture networks where fracture location, size and orientation are sampled from probability density functions (PDFs) (Dershowitz and Einstein 1988; Bour and Davy 1997a; Neuman 2005; Lee et al. 2011; Hyman et al. 2015; Liu et al. 2016). DFNs are increasingly used to represent enhanced geothermal systems (e.g., Kennedy et al. 2021) and for some naturally fractured geothermal systems (e.g., Maffucci et al. 2015; Masri et al. 2015; Ma et al. 2022). DFNs can represent fractures at the scales observed in borehole images, but the high number of fractures and models needed to yield statistically relevant results at reservoir scale is computationally costly (Hyman et al. 2015a; Lei et al. 2017).

DFN input parameters are, if possible, derived from surface analogues and borehole images, and can be challenging to estimate (Berkowitz 2002; Neuman 2005; Lee et al. 2011; Romano et al. 2020). Fracture orientation is the easiest parameter to measure, especially if variations between boreholes are limited. Fracture densities measured in localised, 1-D boreholes must be upscaled to reservoir dimensions in a way that is consistent with the lithological and tectonic contexts. Fracture length, hydraulic aperture

and connectivity are the parameters least constrained from data and need calibration from hydraulic or tracer tests.

This paper presents results from new numerical codes (XFRAC and YFLOW) to generate 2-D fracture networks and model steady-state, isothermal fluid flow in reservoir scale domains ($1 \text{ km} \times 1 \text{ km}$). For the first time, properties of flow through TVZ geothermal reservoir rocks are modelled using DFNs that are calibrated by borehole measurements. The PDFs of bulk flows and flow anisotropy resulting from 1000 DFN realisations are used to calibrate more conventional continuum models of km-scale regions of fractured geothermal reservoirs. Firstly, we present geometric parameters of fractures from borehole images and how they are simplified for model input. Secondly, we present the new codes. Thirdly, we present geometric and hydrological characteristics of the models, compare them with equivalent continuum models (ECMs), and examine hydrodynamic fluid dispersion and the characteristics of tracer particle paths in the models. Finally, we discuss the applicability of these results to geothermal reservoir modelling and engineering.

Summary of earlier findings using XFRAC and YFLOW

Several papers which explored various aspects of 2-D DFNs in fractured TVZ reservoirs preceded the work presented here. Kissling et al. (2015) explored the effects of up to 10 fractures in a $1 \text{ m} \times 1 \text{ m}$ domain with varying aperture, spacing, orientation and in-situ stress, finding that connected fractures can increase permeability by two orders of magnitude. Kissling and Massiot (2017) evaluated the exponent of a truncated power-law distribution for fracture length. They found that an exponent of 2 to 2.5 ensured fractured networks are fully connected on $0.35 \text{ km} \times 0.35 \text{ km}$ model domains, i.e. above the percolation threshold (Bour and Davy 1997), and consistent with TVZ reservoir conditions. Kissling and Massiot (2018) parameterised the hydraulic aperture parameter to fit TVZ reservoir conditions and explore the large variations in residence time through different connected fractured paths. Kissling and Massiot (2019, 2021) evaluated the use of one or several families of fracture orientations to be as close as possible to borehole observations of the Rotokawa Geothermal Field. They showed that a single normal distribution of fracture orientation was adequate based on overall flow and permeability anisotropy behaviour in the $0.35 \text{ km} \times 0.35 \text{ km}$ DFN.

Data and methods

Fracture system characteristics and input into models

Input parameters of the DFNs are chosen to be consistent with borehole observations and are summarised in Table 1. The model domain is $1 \text{ km} \times 1 \text{ km}$. For the purpose of calculating a total mass flow, we assume a model thickness of 0.1 km, over which the DFN does not vary. The DFN input parameters are based on interpretations of acoustic borehole images in three boreholes at the Rotokawa Geothermal Field (hereafter 'Rotokawa') (Massiot et al. 2017a) and four at the Wairakei Geothermal Field ('Wairakei') (McNamara et al. 2019), Aotearoa New Zealand. The borehole deviations range from vertical to deviated by up to 30° towards various azimuths. This configuration decreases sampling biases (Priest 2004; Massiot et al. 2017c). All acoustic borehole images were

Table 1 Summary statistics from borehole images and input parameters for 2-D DFNs

Parameter	Lithologies	Borehole measurements	Input for 2-D models (this study)
Fracture centre location	All	No discerned clustering	Uniform distribution in each of X and Y directions
Orientation	All	Dominant population: Dip magnitude: subvertical ($82^\circ \pm 6^\circ$), dip direction to NW and SE Strike: NE-SW Minor population 1: dip magnitude $67^\circ \pm 12^\circ$ and strike N-S Minor population 2: dip magnitude between 30° and 70° and varied strike	Dominant population: Dip magnitude: Normal distribution, mean = 90° (vertical) and standard deviation = 15° Strike: models are orientated NW-SE, i.e., perpendicular to the measured dominant fracture strike Minor populations: not modelled (see text for explanation)
Linear density (P_{10} , m^{-1})	Sheet-like andesite	0.6 (n = 1405; Length of image = 2334 m)	0.6
	Pyroclastic rocks/ignimbrite	0.8 (n = 648; Length of image = 807 m)	0.8
	Rhyolite lava and breccia	1.7 (n = 826; Length of image = 496 m)	1.7
Length (L, m)	All	Unknown	Doubly-truncated power law PDF: $P(L) = A/L^\lambda$ $A = (1/a - 1/b)$ with: $a = 1$, $b = 100$, $\lambda = 2$; $a \leq L \leq b$
Geometric aperture (a_g , m)	All	Power law PDF: $P(a_g) = A/a_g^\alpha$, $\alpha = 2.6$	$a_g = L/1000$
Volume of fractures and veins per volume of rock (P_{33} , dimensionless)	All	0.01–0.1 at thin section, core and acoustic image scales	0.05 naturally results from choice of a_g
Hydraulic aperture (a_h , m)	All	Unknown	$a_h = \beta L/1000$ with: $\beta = 0.002$

Measurements on borehole images from Massiot et al. (2017a).

acquired with the same acoustic borehole imaging tool (ABI85 developed by Advanced Logic Technology, rated to 300°C).

The lithologies represented in the model are those common in producing geothermal reservoirs in the TVZ (Fig. 1): pyroclastic rocks (at Wairakei), rhyolite bodies comprising lavas and breccias (at Wairakei) and sheet-like andesites (at Rotokawa). Pyroclastic rocks comprise tuffs and non-welded to welded ignimbrites of the Tahorakuri Formation, Waiora Formation and Wairakei Ignimbrite at Wairakei (McNamara et al. 2019). Rhyolite lavas and breccia comprise the Karapiti 2B Rhyolite, Poihipi Rhyolite, rhyolite of the Waiora formation and other rhyolite lavas and andesite dikes that are all small in volume ($< 0.5 \text{ km}^3$) (McNamara et al. 2019). Lavas cannot be differentiated from breccia on either drill cuttings or borehole images. Sheet-like andesites are those of the Reporoa Group andesites comprising the Nga Awa Purua Andesite and Rotokawa Andesite which is $> 1 \text{ km}$ -thick in places with $> 10 \text{ km}$ lateral extension (Milicich et al. 2019). Laboratory measurements of such rock types in New Zealand geothermal reservoirs showed varied petrophysical properties but with low to moderate porosity and low permeability ($< 3 \times 10^{-16} \text{ m}^2$) (Siratovich et al. 2014; Wyering et al. 2014; Cant et al. 2018). In those

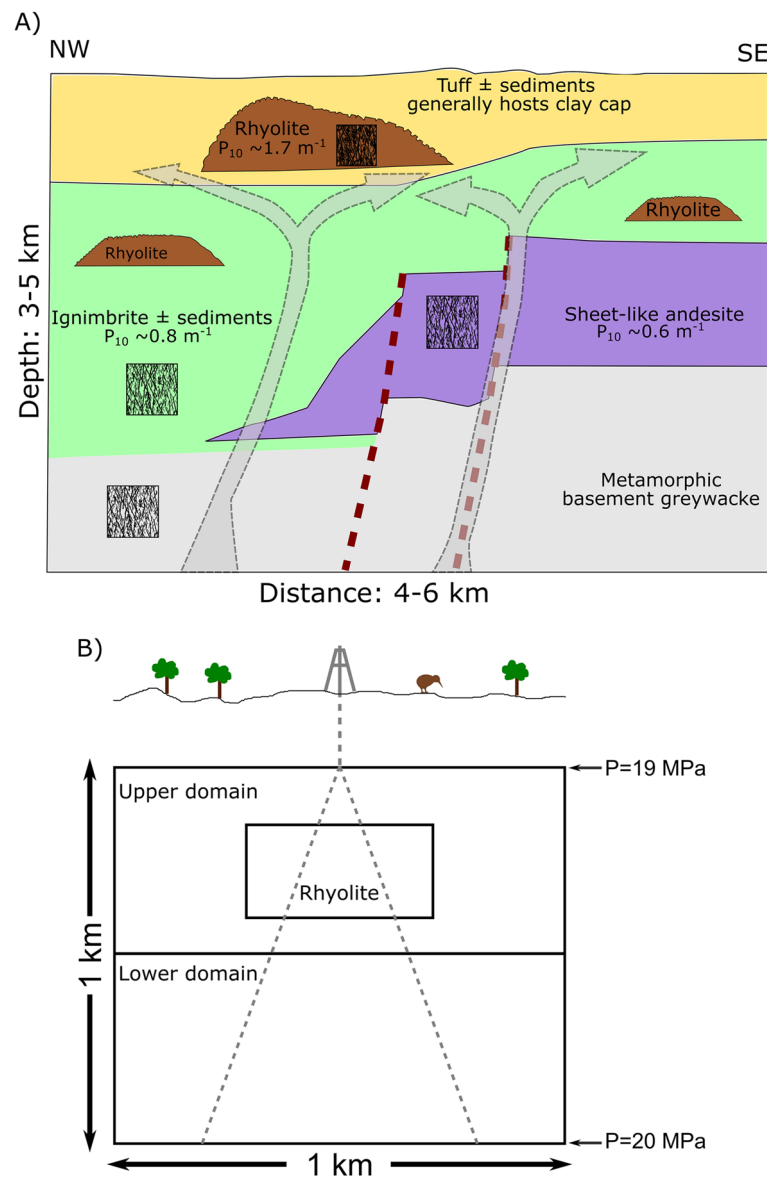


Fig. 1 Model geometry and boundary conditions. **A** Schematic geological cross-section of a TVZ geothermal reservoir loosely based on Rotokawa (McNamara et al. 2016; Milichich et al. 2020); Wairakei (Sepulveda et al. 2012); and Ohaaki (O'Sullivan et al. 2021) geothermal reservoirs. Thick grey arrows are potential upflows and lateral flows in the reservoir. All formations are pervasively fractured. The diagram is oriented NW–SE, i.e. perpendicular to the Taupō Rift and hence perpendicular to the dominant fracture and fault strike. Pervasive fractures are represented on small squares in each rock types. **B** DFN geometry (physical extent 1 km × 1 km) and pressure boundary conditions. Dashed grey lines represent drillholes deviated 20° from the vertical, similar to those in which borehole images used in this paper were collected

reservoir rocks of high-temperature alteration, connected porosity is dominated by microcracks in andesites (mean of 8.4 ± 3.2 vol.%; Siratovich et al. 2014; 5.6 ± 3.9 vol.%, Wyering et al. 2014), and either microcracks, pores or a mix in ignimbrites (12.3 ± 5.3 vol.%, Wyering et al. 2014; 11.7 ± 5.5 vol.%; Cant et al. 2018). In this study, we model flows only through macro-fractures, assuming that the matrix permeability is negligible.

Fracture density

Linear fracture densities along the acoustic borehole images (P_{10} , terminology as per Dershowitz and Herda 1992) were averaged for each of the three considered lithologies. Only intervals with >25% azimuthal borehole coverage were considered, in which most fractures are deemed to be imaged at the tool resolution (Massiot et al. 2017c).

Acoustic borehole images are well suited to provide the input fracture density to evaluate flows in DFNs. Indeed, acoustic borehole images are increasingly acquired in geothermal boreholes (Genter et al. 1997; Davatzes and Hickman 2010; Vidal et al. 2016; Ziegler et al. 2016; Mutonga and Fujimitsu 2021). Resistivity borehole images are also acquired in geothermal fields (Stimac et al. 2008; McNamara et al. 2019; Intani et al. 2020). Although resistivity images usually detect finer (hence more) fractures and lithological details, acoustic images tend to image those fractures most likely to be permeable (Davatzes and Hickman 2010; McNamara et al. 2019).

Fracture spatial distribution

In general, faults and their damage zones result in spatial clustering of fractures (Gillespie et al. 1993; Brathwaite et al. 2001), but this effect has not been clearly observed in the borehole images considered here. At Rotokawa, the fractures were distributed throughout the imaged interval rather than being clustered in specific locations (Massiot et al. 2017a). At Wairakei, high fracture density was linked to a fault damage zone in only one occurrence, while other zones of high fracture density were inferred to be associated with other parameters including lithology and hydrothermal alteration (McNamara et al. 2019). For simplicity in this study, the location of fractures is modelled as random, i.e. without spatial correlation. The models represent the pervasive fracture network *between* the major faults within the geothermal field, as well as some of the faults that do not display the classic clustering in fault zones.

Fracture orientation

Fractures in borehole images at both Rotokawa and Wairakei dominantly strike NE-SW and are steeply dipping, with 75% of fractures having a dip magnitude >70°. These orientations are consistent with the normal faulting regime in the Taupō Rift (Villamor and Berryman 2001). The 2-D models represent a vertical section orientated NW–SE, i.e. fractures strike “out of plane”. The fracture dip magnitudes in the model are described by a normal distribution centred such that the mean fracture direction (MFD) is parallel to the Y direction in the model domain (“vertical”). This configuration applies to parts of geothermal reservoirs where fluid flow is dominantly vertical (Fig. 1).

Detailed fracture orientation analyses of borehole images identified subordinate fracture orientations (Massiot et al. 2017a; McNamara et al. 2015). There was no clear correlation between specific fracture sets and permeability. Kissling and Massiot (2021) found that permeabilities were equivalent in DFNs built using (1) major and subordinate fracture orientations as in the borehole images or (2) a single normal distribution of steeply-dipping fractures. In this study, a single population of fracture orientations is used to explore the effects of varying fracture density while being consistent with borehole image observations.

Fracture length

Fracture lengths are not measurable in boreholes. Here, we assume that fracture length follows a doubly-truncated power-law distribution, with lower and upper limits of fracture length being 1 and 100 m, respectively. The upper bound is consistent with fractures being smaller than reservoir-scale faults, which are commonly > 1 km-long. The lower bound maintains a representative fracture length range of two orders of magnitude (Bonnet et al. 2001) and limits the computational costs of small fractures which are unlikely to provide connectivity on reservoir length scales of ~ 1 km.

The power-law length exponent was explored in Kissling and Massiot (2017). The power-law length exponent used here ($\lambda=2$) yields fracture networks consistent with known reservoir-scale fluid flow behaviour. That is, fluid flow occurs through fractures that are fully connected on ~ 1 km length scales and, with high probability, no significant gaps in the connectivity occur at this scale. This choice is also consistent with power-law exponents measured in a variety of settings worldwide and at various scales such as thin section, core, outcrop, aerial photography and seismic survey. The measurements vary between 1 and 3, but suggest that $\lambda=2$ is a representative value (Bonnet et al. 2001; Torabi and Berg 2011, and references therein).

Fracture geometric and hydraulic apertures

The geometric aperture of a fracture is the distance between the fracture or vein walls measured on borehole images. The geometric aperture in sheet-like andesites at Rotokawa ranges between 1 and 57 mm and is considered unaffected by sampling bias between 9 and 30 mm (Massiot et al. 2017a). There, geometric aperture follows a power-law distribution across drill cores and acoustic images scales with a power-law exponent of 2.6 (Massiot et al. 2017a). Geometric apertures of fractures on acoustic images at Wairakei follow a similar range (McNamara et al. 2019) and distribution.

Based on cores, thin-sections and borehole images at Rotokawa, Massiot et al. (2017a) estimated the fracture porosity (including sealed veins) to be ~ 0.05. Fracture length and geometric aperture are generally correlated (Bonnet et al. 2001). Gudmundsson (2000) estimated a ratio of fracture width to length of 1/400, based on outcrop measurements of mineral-filled veins in basalts. Here, we use a constant ratio of 1/1000 for geometric aperture to fracture length to set the overall fracture porosity to 0.05. In drill cores, fractures and veins are commonly < 1 mm thick (Massiot et al. 2017a), that would correspond to a length of < 1 m. These core-scale fractures and veins are not represented in this study.

The geometric apertures of fractures measured in borehole images are significantly greater than the hydraulic apertures which control the flow of fluids (Barton et al. 2013; Masri et al. 2015). There are two main reasons for this. Firstly, borehole images overestimate the geometric fracture aperture at the borehole walls due to signal scattering at the rough fracture edges (Davatzes and Hickman 2010). Secondly, borehole images measure the fracture thickness between fracture walls, but the hydraulic aperture is much smaller. This is due to at least partial infill by precipitation of alteration minerals (Griffiths et al. 2016; McNamara et al. 2016). On the contrary, dissolution of hydrothermal minerals through change of fluid composition or pressure/temperature conditions and fracture reactivation can increase a fracture's

permeability (Barton et al. 1995; Genter and Traineau 1996), hence hydraulic aperture, at least temporarily. On borehole images, fractures of high acoustic amplitude are considered fully mineralised by quartz or calcite, but those of low acoustic amplitude can be fully open, partially mineralised fractures, or fully mineralised (closed) veins by iron oxide, pyrite and clays (Massiot et al. 2017b; Milloy et al. 2015). In the TVZ reservoirs modelled in this paper, that uses only fractures of low acoustic amplitude, clay and iron oxides alteration are less common than in shallower parts of the reservoirs, so the potential for severing connection would be limited to the effects of pyrite.

To calibrate the relationship between geometric and hydraulic aperture, and consider in a simple way the competing factors that can increase or decrease hydraulic apertures, we use an ‘aperture factor’ β (as described in Kissling and Massiot 2018 and 2019). To define β , the mean vertical flow from an ensemble of DFNs is compared with reservoir-scale permeabilities derived from boreholes testing and modelling. The value of β we use (0.002) relies on the definition that the fluid flux through a fracture network with $P_{10} = 0.6 \text{ m}^{-1}$ is equivalent to that in rock with a bulk vertical permeability of $30 \times 10^{-15} \text{ m}^2$ (Appendix 2). For fracture lengths of 1 and 10 m, this yields hydraulic apertures of $2 \cdot 10^{-6}$ to $2 \cdot 10^{-4} \text{ m}$, respectively. This hydraulic aperture range is similar to those derived from well test and microseismic data during stimulation of the Habanero (Australia) and Wayang Windu (Indonesia) geothermal fields (Barton et al. 2013; Masri et al. 2015). This bulk permeability value is also used in comparison of DFN and equivalent continuum models (ECMs) in Sect. “[Pressure distribution within the DFNs and comparison with continuum models](#)”.

Codes and algorithms

The new code used in this study comprises two parts: XFRAC and YFLOW (see flow chart, Fig. 10 in Appendix 1). XFRAC creates 2-D fracture networks using statistical descriptions of fracture networks derived from acoustic borehole imaging. YFLOW then calculates the total fluid flow through these networks. Both codes are written in Fortran90 and compiled using an Intel compiler. XFRAC uses OpenMP (included in the compiler) to create independent realisations of the fracture networks which run simultaneously on multiple threads. XFRAC requires uniformly distributed random numbers to generate properties of individual fractures and their distribution in the model domain, and these are generated using the Fortran90 intrinsic subroutine RANDOM_NUMBER. YFLOW uses the PARDISO linear algebra library (Bollhöfer et al. 2019, 2020; Alappat et al. 2020; Schenk and Gärtner 2020) to solve for the pressure at each node/fracture intersection in the model. YFLOW also requires uniform random numbers for particle tracing.

Fracture generation codes XFRAC and YFLOW

XFRAC is designed to extrapolate fracture information from the borehole images to a reservoir-scale model domain. XFRAC builds fracture networks that match the input values of P_{10} in any model subdomains penetrated by virtual boreholes with a specified

angle of deviation from vertical. YFLOW calculates the flow through the fracture network generated in XFRAC when a pressure gradient is applied across that domain.

These codes are written with geothermal reservoir engineers in mind. As with most reservoir engineering tools (e.g. Grant and Bixley 2011) approximations are made to expedite analysis, and so highly-complex non-linear problem formulations have been avoided. Assuming isothermal conditions and constant fluid properties, the resulting sparse linear systems of equations with several hundred thousand unknown nodal pressures are easily handled with modern linear algebra packages. Without this linearity, the calculation of the properties of ensembles of fracture networks, as described in this paper, would be much more difficult.

The fracture network generated by XFRAC is reduced to its equivalent backbone network (BBN), i.e., that network containing only fractures which provide continuous, connected paths for fluid transport across the model domain. To do this, fractures which are a) connected to only one other fracture, and b) do not intersect the boundary of the model domain, are successively removed. This is an iterative process because removing some fractures will in many cases expose others which are singly-connected. Convergence to the BBN continues until there are no remaining singly-connected fractures, and generally occurs within approximately ten iterations.

YFLOW calculates the flow through the BBN. A flow law describes the mass flux through any fracture segment as a function of the hydraulic aperture and the pressure gradient in that segment. In this paper we use the ‘cubic law’ (e.g. Boussinesq 1868; Zimmerman and Bodvarsson 1996), where the flow rate through the segment is proportional to the cube of the hydraulic aperture multiplied by the pressure gradient in that segment. The condition that the flows into (or out of) any node must sum to zero for a steady state gives the necessary linear relation between the pressures at a node and those nodes directly connected to it. When assembled for all nodes in the BBN, these linear equations can be solved for the pressures at all the nodes.

YFLOW can also trace the paths taken by fluid through the fracture networks. Because fluid mass is conserved at each fracture intersection, there are only three possible paths for a fluid particle to take at any intersection (Fig. 2). Fluid can enter the intersection from either 3, 2 or 1 fractures (Fig. 2A–C, respectively), and then can only leave by 1, 2 or 3 fractures in each of these cases. In the particle tracing algorithm, the probability of a fluid particle leaving by one of the exit fractures is assumed to be proportional to the magnitude of the flow in that fracture, with the sum of the probabilities always being one.

As an example, suppose there is one inflow and three outflows with respectively 1, 3 and 6 kg/s in left, top and right fractures (consistent with Fig. 2C). The probability of a tracer particle taking the left-hand, top or right-hand pathways are 0.1, 0.3 and 0.6 respectively. In other words, 10% of the fluid entering the intersection will leave by the left pathway, 30% through the top pathway, and 60% by the right pathway. The choice of path is made by sampling a random variable from a uniform [0, 1] probability distribution and determining which of the three ranges [0.0–0.1], [0.1–0.4] or [0.4–1.0] it lies in.

Validation of the codes XFRAC and YFLOW is demonstrated in Appendix 2 using a simple network and comparing the results from the codes to an analytical solution.

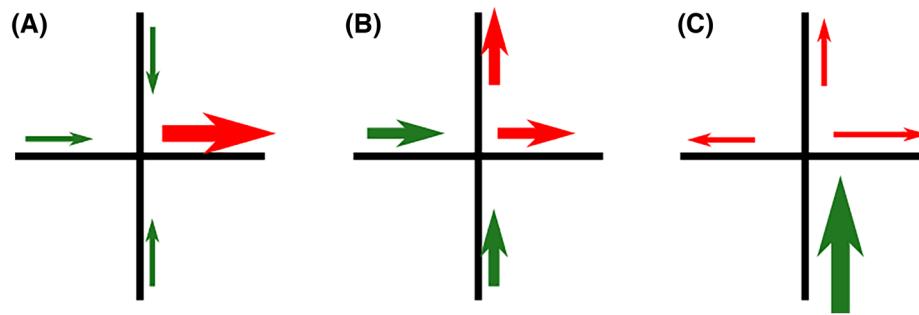


Fig. 2 Possible pathways when fluid tracer particles reach the intersection of two fractures (horizontal and vertical black lines). Green arrows represent inflows to the intersection and the red arrows outflows. The arrow thickness represents magnitude of flows. For any fluid particle entering the intersection, the probability of it leaving by any outflow pathway is proportional to the flow in that pathway

Table 2 Summary of models and input linear fracture densities; $P_{10}=0.6 \text{ m}^{-1}$ in sheet-like andesites, $P_{10}=0.8 \text{ m}^{-1}$ in ignimbrites, $P_{10}=1.7 \text{ m}^{-1}$ in rhyolite lavas and breccia

Model	P_{10} lower sub-domain	P_{10} upper sub-domain	P_{10} rhyolite lava and lava size	Continuum models	Fluid particle tracing
A	0.6	0.6	–	Yes	Yes
B	0.6	0.8	–	Yes	
C1	0.6	0.8	1.7 (0.25 km \times 0.1 km)		
C2	0.6	0.8	1.7 (0.5 km \times 0.25 km)	Yes	
D	0.8	0.6	–	Yes	
E	0.8	0.8	–		
F	0.5	0.5	–		
G	0.4	0.4	–		
H	0.3	0.3	–		
I	0.2	0.2	–		

P_{10} is the same in upper and lower sub-domains in Models A, E–I. The dimensions of all models are 1 km \times 1 km. Flows calculated for all models; continuum models and particle tracing conducted only for models labelled “Yes”.

Model set-up, boundary conditions and reported quantities

In this paper we present simulation results for 10 models (Fig. 1, Table 2). Models A and E–I have constant fracture density over the entire 1 km \times 1 km domain. In Models A ($P_{10}=0.6 \text{ m}^{-1}$) and E ($P_{10}=0.8 \text{ m}^{-1}$) the entire domains are populated with a single rock type, sheet-like andesite and ignimbrite, respectively. In models B and D, the region is divided horizontally into upper and lower sub-domains representing units of sheet-like andesites and ignimbrites, and vice-versa. In models C1 and C2 bodies of rhyolite lava and breccia of two different sizes are embedded within the ignimbrite.

Pressure boundary conditions are applied at all positions where fractures cross the boundary of the model domain, and all boundaries therefore allow free flow of fluid. The pressures are set at 20 and 19 MPa on the lower and upper boundaries, respectively (Fig. 1), resulting in a 1 MPa pressure difference over 1 km to drive fluid flow. On the two lateral boundaries the pressure falls linearly from 20 to 19 MPa. Because of the fixed pressures on the lateral boundaries, the near-boundary pressure contours are modified in models where P_{10} (or equivalently, the permeability) changes within the model domain. The applied pressure gradient of 1 MPa per km is used to accentuate

these boundary effects to provide a more stringent comparison between fracture and continuum models (Sect. “[Pressure distribution within the DFNs and comparison with continuum models](#)”). In New Zealand geothermal systems, reservoir-scale pressure gradients are much lower, typically $\sim 0.1\text{--}0.2$ MPa per km (e.g. Wooding 1978, McNabb and Dickinson 1995), but results presented here remain applicable because the models are assumed to be isothermal, implying that fluid properties are constant.

Fluid density and dynamic viscosity are required for the flow calculations. These are held constant in the flow calculation and must be representative of conditions at approximately 2–3 km depth in the geothermal systems. We use $P=20$ MPa and $T=320$ °C, for which fluid (pure water) density $\rho=692$ kg.m⁻³ and dynamic viscosity $\mu=87.4 \times 10^{-6}$ Pa s.

Two flow calculations are performed for each model, with the pressure gradient applied firstly parallel to the MFD and then perpendicular to it. In each case, two components of the flow are calculated—that aligned with the pressure gradient and that perpendicular to it. We refer to the flows aligned with the pressure gradient as the ‘along flows’ when the pressure gradient is parallel to the MFD and ‘across flows’ when perpendicular to it. This nomenclature is illustrated in Fig. 5D. The permeability anisotropy is defined as the ratio of along flows and across flows, as per Lang et al. (2014). In all models the components of flow perpendicular to the pressure gradient are small and average to zero when summed over a large number of realisations.

To represent the inherently stochastic nature of the fracture networks our model results are reported using probability distribution functions (PDFs). For each model (Table 2), we generate (nominally) 1000 (5000 for Model I) statistically identical realisations of each fracture network. The number of fractures in the BBN, the mean ‘along’ flow, and the permeability anisotropy are reported as PDFs. These probability distributions can be used to populate ECMs (Sect. “[Particle tracing and fluid dispersion at reservoir scales](#)”) which are commonly used by the geothermal reservoir engineering community to understand and manage geothermal systems.

Computational details

Computational time for models with the highest number of fractures (e.g., model E: 480,000 fractures and 530,000 intersections) including time for generating individual fracture networks, stripping these back to backbone networks and calculating the flows is approximately two hours per realisation per core (Xeon 6248R 2.4 GHz CPU). The largest models, A-E, typically required between 7 and 15 days to complete 1000 model realisations on 10 cores. Less densely populated models (e.g., model H with 180,000 fractures and 46,000 intersections) required approximately five days to complete 1000 realisations. Tracing of 10,000 fluid particles through a single realisation of model A took approximately four hours.

The number of operations for assembly of the backbone fracture network scales approximately as the square of the number of fractures. We use OpenMP to run multiple realisations of the models simultaneously, though this is limited to about 10 simultaneous realisations by memory constraints.

Results

Fracture system characteristics

For all models, the number of fractures in both the original and backbone networks scale roughly linearly with P_{10} (Fig. 3A). For high density networks ($P_{10} \geq 0.6 \text{ m}^{-1}$), the BBNs contain approximately 30–40% of the fractures in the original network (Fig. 3A). The number of fracture intersections in the BBN also scales linearly with P_{10} , and with greater slope than the number of fractures (Fig. 3B).

All models with $P_{10} \geq 0.3 \text{ m}^{-1}$ are fully connected in both X and Y directions and adequate statistics can be obtained with 1000 realisations of each model (Fig. 4A). In contrast, fully connected fracture networks are much rarer for Model I ($P_{10} = 0.2 \text{ m}^{-1}$), i.e., networks which are close to or below the percolation threshold. To compensate for this, we generated 5000 realisations of Model I. Approximately 35% of the realisations are fully connected in the Y direction, but only 0.1% are fully connected in both X and Y directions. Typically, the backbone networks are characterised by irregular regions of relatively dense fracturing separated by fracture-less voids with poor or non-existent X-direction connectivity (Fig. 4B, D). Some networks are not fully connected in either X or Y direction (Fig. 4B), while others are fully connected in the Y-direction but contain distinct groups of fractures which are not connected in the X direction (Fig. 4C). Other networks can be more densely populated with smaller areas free of fracturing, but are nevertheless fully connected in both X and Y directions (Fig. 4D). The example in Fig. 4D is particularly extreme: the network consists of two large, connected groups where X-connectivity is provided by just a single fracture (at approximately $X = 300 \text{ m}$, $Y = 700 \text{ m}$).

Permeability and permeability anisotropy

Mean flows along the pressure gradient scale linearly with P_{10} for all models above the percolation threshold ($P_{10} \geq 0.3 \text{ m}^{-1}$) (Fig. 5A). As expected, the flows are greater when the pressure gradient is parallel to the mean fracture direction than when it is perpendicular to (across) it. The mean permeability anisotropy increases from 10 to 13 for $P_{10} \geq 0.3 \text{ m}^{-1}$ (Fig. 5B), though the increase remains well within the uncertainties over the whole range of P_{10} . For P_{10} in the range $0.6\text{--}0.8 \text{ m}^{-1}$, the standard deviation of the permeability anisotropy is ~ 1 (Table 3). These standard deviations increase for lower P_{10} because of the increased variability which occurs with lower fracture densities. For $P_{10} = 0.2 \text{ m}^{-1}$, fully connected BBNs are so rare (5 cases in 5000 realisations) that the calculated standard deviations are not robust, but we note that the mean permeability anisotropy in these cases ranges approximately from 3 to 8 (Fig. 5).

The equation in Fig. 5A for total mass flow (Q_t) through the model domain can be adapted to predict permeability because the models are calibrated so that $P_{10} = 0.6 \text{ m}^{-1}$

(See figure on next page.)

Fig. 3 Fracture statistics as a function of input P_{10} . **A** Number of fractures before and after trimming the unconnected fractures to form the backbone network. Note that the line for the backbone fractures reaches the zero fractures at $P_{10} \sim 0.2 \text{ m}^{-1}$, thus defining the percolation threshold. Letters in brackets refer to model names (Table 2). **B** Number of fracture intersections in the backbone network. Error bars: 3 standard deviations either side of the mean. Models B and D overlap. The vertical axes in each plot in units of thousands (10^3). Linear regressions for all models except C1 and C2

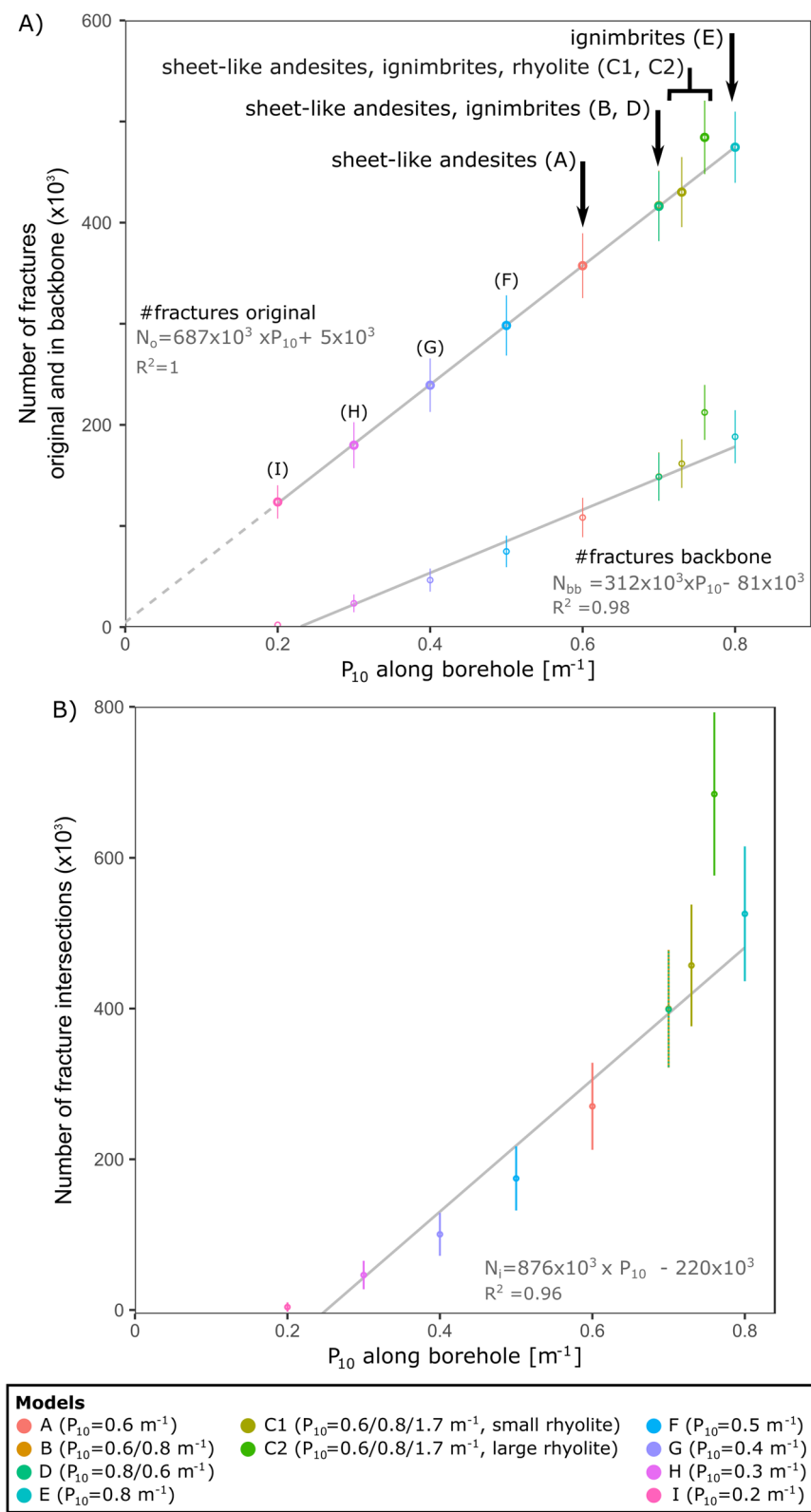


Fig. 3 (See legend on previous page.)

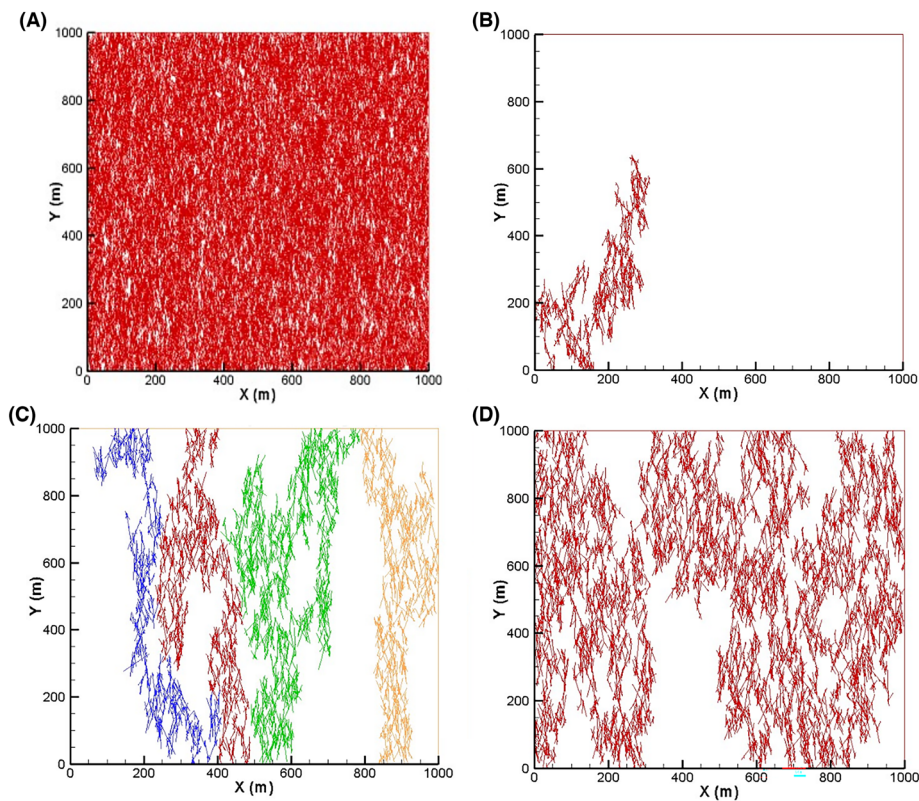


Fig. 4 Examples of backbone fracture networks. **A** Model A, $P_{10}=0.6 \text{ m}^{-1}$ **B–D**: networks close to the percolation threshold (Model I, $P_{10}=0.2 \text{ m}^{-1}$). **B** Network not connected across the model domain in either X or Y direction (approximately 65% models). **C** Strongly channelled network supporting flow only in the Y direction (approximately 35% of models). Each of the four channels is displayed in a different colour. **D** Network connected across the model in both directions (0.1% of models)

corresponds to a permeability of $k=30 \times 10^{-15} \text{ m}^2$. The total mass flow through the cross-sectional area of the models ($1000 \text{ m} \times 100 \text{ m} = 10^5 \text{ m}^2$, A) is:

$$Q_t = 66 P_{10} - 16 \text{ kg s}^{-1} \quad (1)$$

It is more natural to work in terms of the mass flux Q_f (mass flow per unit area), i.e. $Q_f = Q_t/A$. So, for $P_{10}=0.6 \text{ m}^{-1}$: $Q_f = 10^{-5}(66 \times 0.6 - 16) \text{ kg m}^{-2} \text{ s}^{-1} = 23.6 \times 10^{-5} \text{ kg m}^{-2} \text{ s}^{-1}$

We define a conversion factor C to directly convert a measurement of P_{10} to a permeability k :

$$k = C Q_f \quad (2)$$

For the ‘calibration values’ of $Q_f = 23.6 \times 10^{-5} \text{ kg m}^{-2} \text{ s}^{-1}$ and $k = 30 \times 10^{-15} \text{ m}^2$, the conversion factor between mass flux and permeability is: $C = 1.27 \times 10^{-10} \text{ m}^4 \text{ s kg}^{-1}$.

As an example, $P_{10}=0.8 \text{ m}^{-1}$ yields a mass flux $Q_f = 36.8 \times 10^{-5} \text{ kg m}^{-2} \text{ s}^{-1}$ and a permeability $k = 46.7 \times 10^{-15} \text{ m}^2$. The permeability k is zero for $P_{10} \leq 0.24 \text{ m}^{-1}$, consistent with modelling results (Fig. 5A).

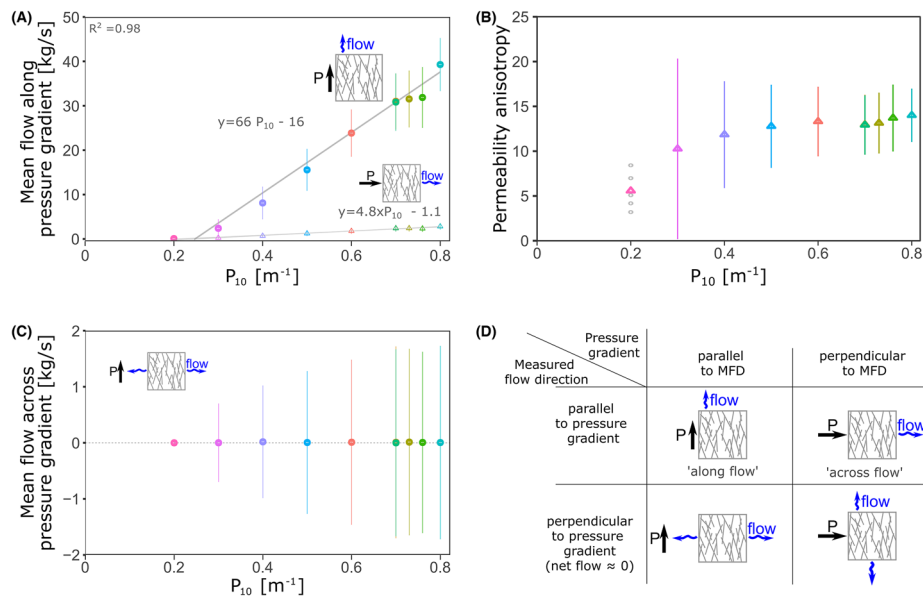


Fig. 5 **A** Flow properties parallel to the pressure gradient as a function of P_{10} . As expected, the flows with the pressure gradient parallel the mean fracture direction are greater than those when the pressure gradient is across it. **B** Permeability anisotropy, defined as the ratio of the two flows illustrated in panel A. No meaningful error bars can be given for Model I ($P_{10} = 0.2 \text{ m}^{-1}$) because only 0.1% of networks have non-zero flows in both X and Y directions. **C** Mean flow perpendicular to the pressure gradient (in case where it is parallel to the MFD) is consistent with zero, as expected. **D** Schematic representation of pressure gradient, measured flow direction and mean fracture direction (MFD). Flows are 'bulk', i.e. the sum of many flows from individual fractures at each boundary. Flows in both directions are possible at each boundary but the arrows indicate the net effect. Error bars: 3 standard deviations

For practical use in other geothermal systems the conversion factor C must be scaled by the inverse of the applied pressure gradient. This operation guarantees that the calculated permeability will depend only on P_{10} , regardless of the pressure gradient. Indeed, Q_f itself is proportional to the pressure gradient. The factor C also depends on ρ/μ . However, the relevant combination of thermo-physical properties of water (ρ/μ) in any high-temperature system (250–320 °C) differ by less than 10% from the values used in this paper, well within the margins of uncertainty for reservoir engineering purposes. For temperatures as low as 200 °C, the difference is 25%.

The net flow perpendicular to the pressure gradient is expected to be very small in the two configurations where the pressure gradient is either aligned with or parallel to the MFD. This is indeed the case: flows across the pressure gradient are typically two to three orders of magnitude smaller than those aligned with the pressure gradient (Fig. 5C, Table 3).

The number of fractures in the original and backbone networks are represented by near-normally distributed PDFs for all models (Fig. 6A; Additional files 1, 2, 3, 4, 5, 6, 7). The mean flow along the pressure gradient is also represented by near-normal distributions for models with $P_{10} \geq 0.3 \text{ m}^{-1}$ (Fig. 6B). Permeability anisotropy similarly follows a near-normal distribution for models with $P_{10} \geq 0.5 \text{ m}^{-1}$. Permeability anisotropy for models with $P_{10} = 0.3$ to 0.4 m^{-1} (Models G and H) become increasingly skewed with increased standard deviation (Fig. 6C, Table 3).

Table 3 Summary statistics of DFN model realisations. Numbers reported as mean \pm 1 standard deviation

Model	Number of fractures or intersections				Flows (kg.s ⁻¹)			Anisotropy
Model	Mean P ₁₀ (m ⁻¹)	Original	Backbone	Intersections	Pressure gradient parallel to mean fracture direction		Pressure gradient perpendicular to mean fracture direction	
					Flow parallel to MFD (Fig. 5A)	Flow perpendicular to MFD (Fig. 5C)	Flow perpendicular to MFD (Fig. 5A)	
A	0.6	3.6e+05 ± 1.1e+04	1.1e+05 ± 6.5e+03	2.7e+05 ± 1.9e+04	23.8 ± 1.8	0.011 ± 0.49	1.81 ± 0.21	0.0026 ± 0.19
B	0.7	4.2e+05 ± 1.2e+04	1.5e+05 ± 8.0e+03	4.0e+05 ± 2.6e+04	31 ± 2.1	0.009 ± 0.57	2.41 ± 0.24	0.0026 ± 0.22
C1	0.73	4.3e+05 ± 1.2e+04	1.6e+05 ± 8.0e+03	4.6e+05 ± 2.7e+04	31.5 ± 2.1	0.013 ± 0.55	2.42 ± 0.24	0.0064 ± 0.22
C2	0.76	4.8e+05 ± 1.2e+04	2.1e+05 ± 9.1e+03	6.8e+05 ± 3.6e+04	31.9 ± 2.3	0.007 ± 0.54	2.34 ± 0.24	− 0.0029 ± 0.22
D	0.7	4.2e+05 ± 1.1e+04	1.5e+05 ± 7.9e+03	4.0e+05 ± 2.6e+04	30.8 ± 2.2	0 ± 0.56	2.4 ± 0.24	0.0092 ± 0.21
E	0.8	4.7e+05 ± 1.2e+04	1.9e+05 ± 8.7e+03	5.3e+05 ± 3.0e+04	39.3 ± 2	0.005 ± 0.57	2.82 ± 0.24	0.0094 ± 0.23
F	0.5	3.0e+05 ± 9.9e+03	7.5e+04 ± 5.2e+03	1.7e+05 ± 1.4e+04	15.6 ± 1.6	0.006 ± 0.42	1.23 ± 0.18	0.0047 ± 0.16
G	0.4	2.4e+05 ± 8.8e+03	4.6e+04 ± 3.8e+03	1.0e+05 ± 9.5e+03	8.1 ± 1.2	0.018 ± 0.33	0.7 ± 0.14	0.0075 ± 0.13
H	0.3	1.8e+05 ± 7.6e+03	2.3e+04 ± 2.9e+03	4.6e+04 ± 6.3e+03	2.4 ± 0.7	0.001 ± 0.23	0.25 ± 0.09	0.0007 ± 0.09
I	0.2	1.2e+05 ± 5.5e+03	2.1e+03 ± 1.1e+03	3.9e+03 ± 2.1e+03	0.1 ± 0.1	0 ± 0.02	0.01 ± 0.02	0.0001 ± 0.02
								5.57 ± 2.13

1000 realisations per model, except for model I where 5000 realisations were run. The permeability anisotropy in the final column is the ratio of the along flow to the across flow.

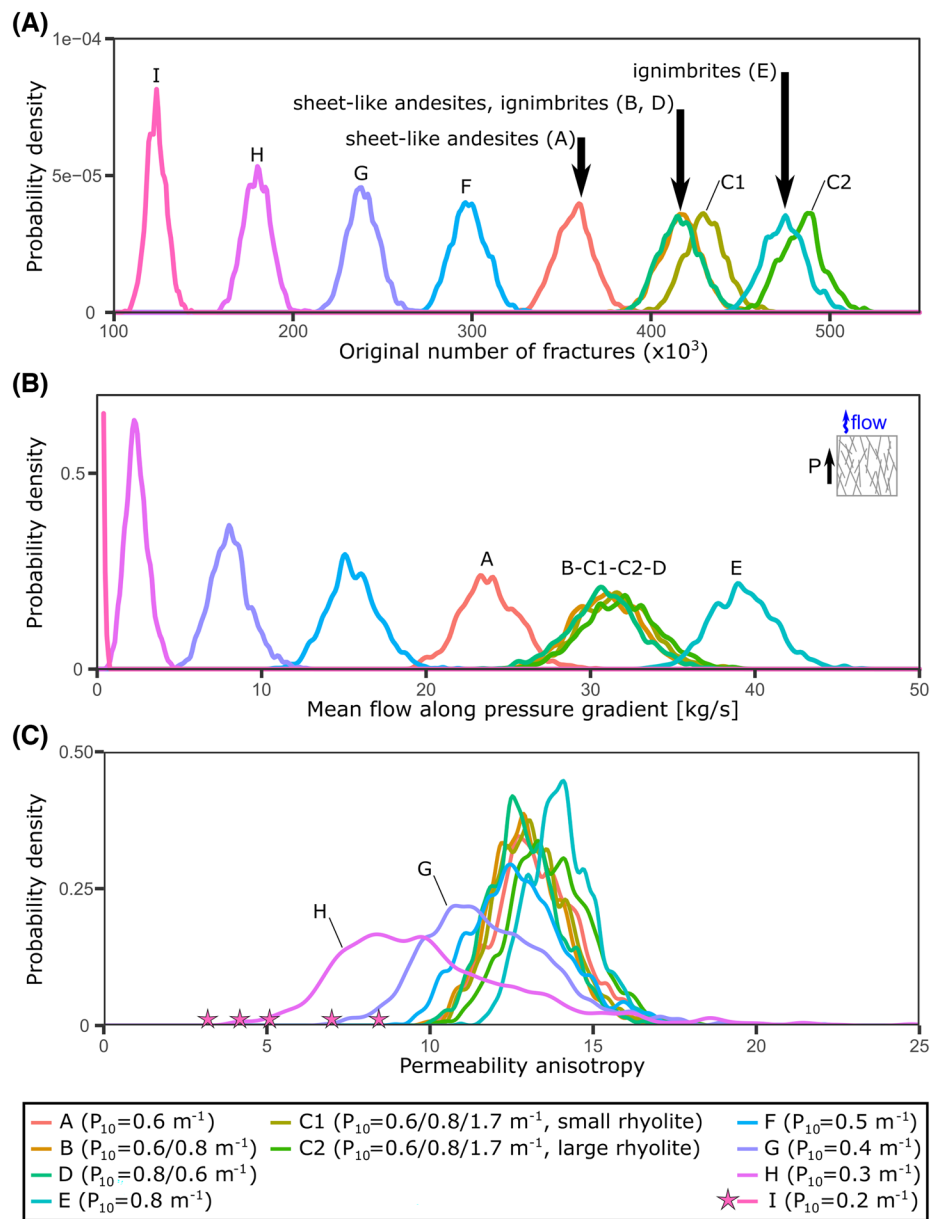


Fig. 6 Probability density functions (PDFs) of **A** number of fractures in the backbone networks for all models, **B** mean flow along the MFD with pressure gradient aligned in the same direction and **C** permeability anisotropy. For model I, the PDF for the permeability anisotropy cannot be sensibly defined because only 5 networks (0.1%) have non-zero flows in both X and Y directions (labelled with a star for each network)

Models C1 and C2 contain densely fractured ($P_{10}=1.7 \text{ m}^{-1}$) rhyolite bodies yet the distributions of mean flow and permeability anisotropy are not perceptibly different from model B, which has the same ignimbrite/andesite distribution but no rhyolite body (Fig. 6B, C). The reason for this is that the rhyolite bodies do not connect the upper and lower boundaries of the model domain and so the derived flows and permeability anisotropy do not respond to the pressure difference prescribed across it. If this were the case the mean flows would increase in proportion to the additional fracture density within the rhyolite and the width of that body. The PDF for Model

Table 4 Summary of permeability calculations for equivalent continuum models (ECMs)

Component	P_{10} (m^{-1})	Number of fractures per km^2 in BBN ($\times 10^3$)	Ratio of BBN fractures per km^2 (andesite = 1)	Y component permeability (10^{-15} m^2)	X component permeability (10^{-15} m^2)
Sheet-like andesite	0.6	106	1.00	30.0	2.31
Ignimbrite	0.8	169	1.59	47.6	3.66
Rhyolite	1.7	449	4.23	126.9	9.77

The number of fractures in the BBNs are calculated using the formula in Fig. 3

D in Fig. 6B is also indistinguishable from models B, C1 and C2. This is expected as Models B and D have identical but ‘reversed’ lithologies where the ignimbrite and andesite units are exchanged. Variations of permeability within the model domain are explored in Sect. “[Pressure distribution within the DFNs and comparison with continuum models](#)”.

Pressure distribution within the DFNs and comparison with continuum models

For comparison with the fracture models, equivalent continuum heat and fluid flow transport models (ECMs) were created with the code TGNS (Kissling 2014). The ECMs used a 100×100 array of grid blocks covering the same $1 \text{ km} \times 1 \text{ km}$ model domain as the DFNs. ECMs were created for Models A, B, D and C2, and were run to a long-time steady state where the calculated pressure distribution remains unchanged.

The X and Y components of permeability (k_x and k_y , respectively) for each ECM are calculated as follows (see summary in Table 4):

1. k_y for $P_{10}=0.6 \text{ m}^{-1}$ is obtained by matching the total mass flow through the domain of model A and its equivalent ECM. For this calculation we use the mean mass flow derived from the 1000 realisations of Model A (23.85 kg s^{-1} , Table 3). Because P_{10} is constant over the model domain the boundary effects discussed in Sect. “[Model set-up, boundary conditions and reported quantities](#)” are absent and this flowrate must correspond to $k_y = 30 \times 10^{-15} \text{ m}^2$ (Sect. “[Fracture spatial distribution](#)”).
2. for lithologies with different P_{10} , k_y is obtained by scaling the permeability from (1) according to the areal density of fractures for BBNs calculated using the formula in Fig. 3A.
3. for each P_{10} , k_x is calculated by dividing k_y from (2) by the permeability anisotropy. We adopt a permeability anisotropy of 13 for all lithologies, consistent with models with $P_{10} \geq 0.6 \text{ m}^{-1}$ (Table 3, Fig. 3B).

For a single realisation of any fracture model, the pressure distribution is calculated by summing and averaging pressures at all fracture intersections within each $10 \text{ m} \times 10 \text{ m}$ square corresponding to the $10 \text{ m} \times 10 \text{ m}$ ECM grid blocks.

As Model A has a single P_{10} throughout the model domain, the pressure distribution in the ECM is linear in the Y direction and independent of the X coordinate (Fig. 7). In models B and D, with two sub-domains, the ECM pressure gradients are lower in the sub-domain with the highest P_{10} , and vice-versa. This is a consequence of the continuity of the mass flow in the model, which requires that the product of the pressure gradient

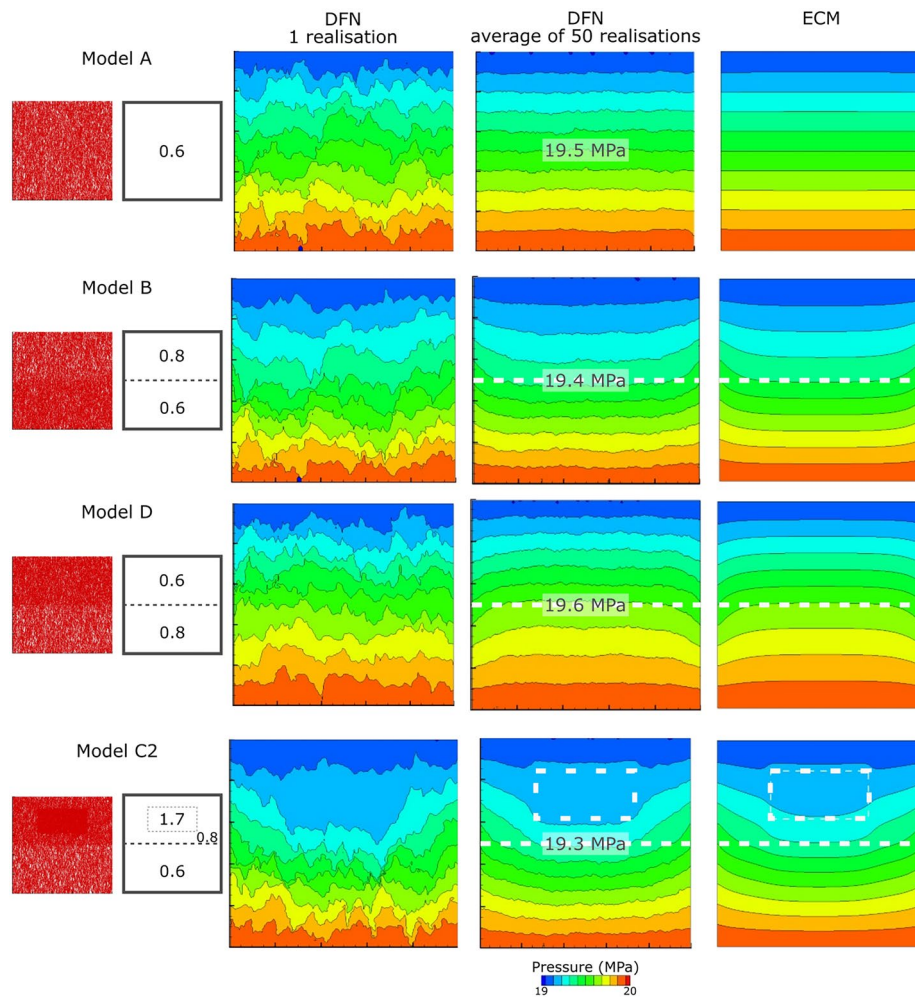


Fig. 7 Comparison of pressure distributions in continuum and DFN models for, from top to bottom rows: models A, B, D and C2. From left to right: example of backbone network; input P_{10} ; DFN with 1 realisation; average of 50 DFN realisations; Equivalent Continuum Models (ECM). The white dashed lines on the plots for Models B, D and C2 indicate changes in lithology in the models

and the permeability k_y be the same in each subdomain. For model C2 a rhyolite body with high P_{10} ($P_{10} = 1.7 \text{ m}^{-1}$) is embedded in the ignimbrite ($P_{10} = 0.8 \text{ m}^{-1}$). This ECM for Model C2 shows a very low pressure gradient and consequently widely spaced contours within the rhyolite.

The pressure boundary conditions on the lateral boundaries are automatically satisfied in Model A, but not for Models B, D and C2. For these ECMs, pressure contours must curve near the lateral boundaries to match the prescribed boundary conditions. For Model B, the higher pressure gradient in the lower subdomain results in a larger pressure drop in that subdomain than in Model A. The pressure contours must then curve upward to match the lateral boundary pressures. The opposite occurs for the same reasons in Model D. For model C2 the boundary effects are similar to model B because the ‘underlying’ P_{10} values are the same in both models, but with additional ‘flattening’ of the upper subdomain boundary pressures due to the proximity of the high P_{10} rhyolite body.

The pressure distributions for single realisations of the DFNs (Fig. 7) are very irregular, reflecting the inherent randomness in those fracture networks. The single-DFN pressure distributions for Models B, D and C2 show weak signs of both the pressure boundary effects and the variations of contour spacing due to lithology changes seen in the ECMs. By contrast, the pressure distributions resulting from averages of 50 DFN realisations are much smoother than the single realisations and closely resemble their corresponding ECMs in all cases.

The pressure distribution directly relates to permeability: zones of lower pressure gradient correspond to higher permeabilities. The calculated mean flows (Table 3) for models B, C1 and C2 are very consistent and the pressure distributions in Fig. 7 mirror each other, with wider spacing of the contours in the region of highest fracture density. The white dashed lines, which indicate changes in lithology, support this. These show smaller pressure change between the lower boundary and the midpoint of the model at $Y=500$ m ($20.0 - 19.6 = 0.4$ MPa) in model D compared to that in Model B ($20.0 - 19.4 = 0.6$ MPa). So, while the total mean flows over the entire domain are similar for models B, C1 and C2, the distribution of pressure are different within the domain and reflect increased permeability in more densely fractured rocks.

Particle tracing and fluid dispersion at reservoir scales

Evaluating fluid dispersion through a geothermal fractured reservoir is important for interpreting tracer tests and hence for efficient reservoir management (Grant and Bixley 2011; Buscarlet et al. 2015; Addison 2015). Tracer tests are acknowledged to be difficult to interpret because continuum porous media-based models cannot account for the multiplicity of paths that fluid particles can take to travel across the model domain. Here, we describe the macroscopic fluid dispersion process that occurs in fracture network. A full evaluation of hydrodynamic dispersion for accurate tracer test interpretation also requires considering the molecular diffusion which occurs within individual fractures (Zhao et al. 2010).

Figure 8C shows the paths of 10,000 tracer particles through one realisation of Model A, commencing at a single-entry fracture near the centre of the lower boundary of the domain. The tracer particles follow a variety of overlapping paths to reach the upper boundary. The nodes where they exit are spread between (X coordinate =) 344 and 631 m, and are generally aligned with the MFD (Fig. 8B). The spread of exit nodes (287 m) gives a crude measure of the hydrodynamic dispersion of fluid that takes place in the geothermal reservoir.

The lateral distribution of tracer particles exiting at the top of the model is uneven within this range. Half of the 10,000 particles exit between 503 and 537 m, while very few particles exit between 480 and 500 m and 540–560 m (Fig. 8A and B). Overall, 44% (71 of 163) of the fractures between 344 and 631 m do not host exiting tracer particles. The presence of heavily fractured regions with and without exiting tracer particles indicates that the flow is heterogeneous. This may explain some occurrence of high and poor tracer returns in nearby boreholes, even in well-connected fractured reservoirs.

Tracer particles take varied times to travel across the domain due to the variety in individual paths (Figs. 8A and 9A). Tracer particles arrive at the upper boundary between 0.6

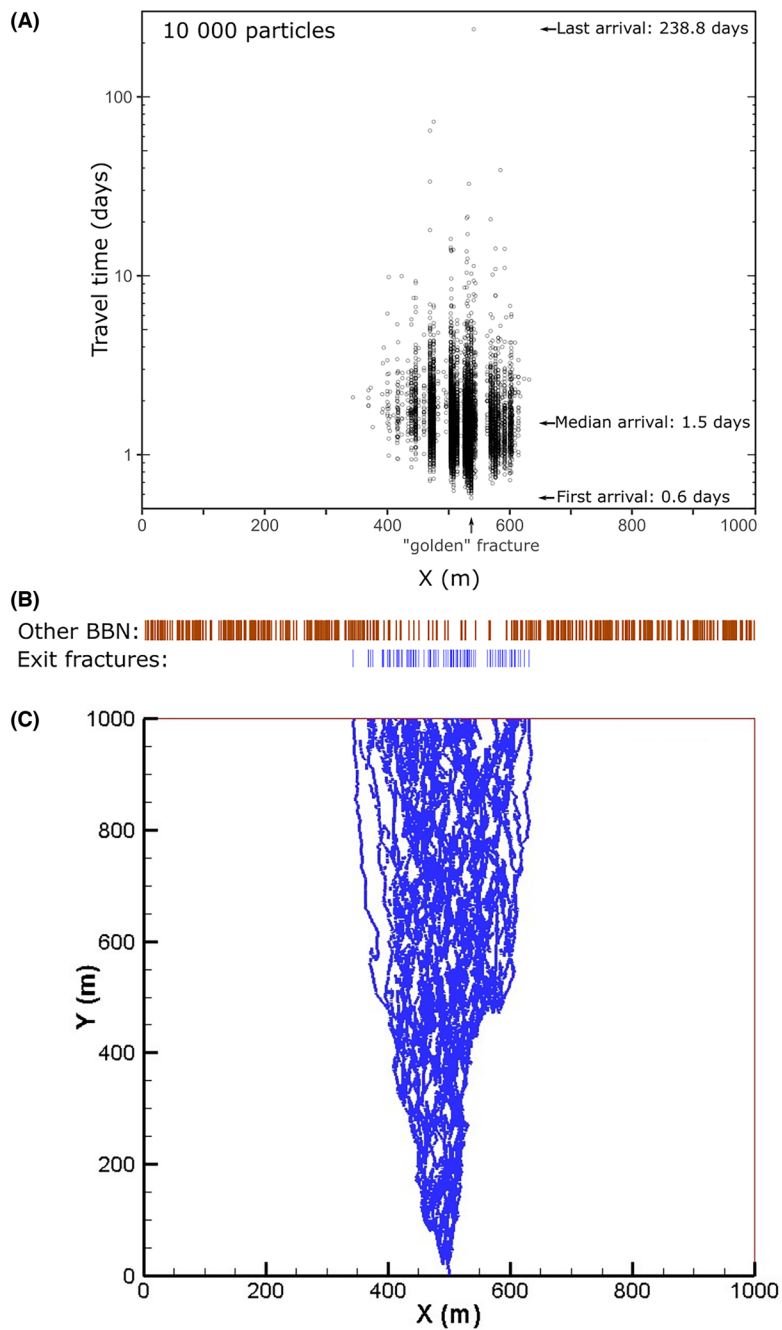


Fig. 8 Tracing of 10,000 fluid particles through one realisation of Model A. **A** Travel time of particles from lower to upper model boundary as a function of coordinates along the X axis. 50% particles exit the upper boundary between 1.2 and 1.7 days, and through fractures located between $X=503$ m and $X=537$ m. "golden fracture": fracture through which 10% of the tracing particles exit. Time axis is in logarithmic scale. **B** Location of fractures through which particles exit the model, and other fractures from backbone network crossing the upper boundary ($Y=1000$). The particles leave the upper boundary through 92 fractures spread over 287 m. In this interval, 71 fractures do not host exiting fluid particles. In all, 550 fractures intersect the upper boundary of the model domain. **C** Paths taken by fluid particles which enter the model domain through a single fracture on the lower boundary

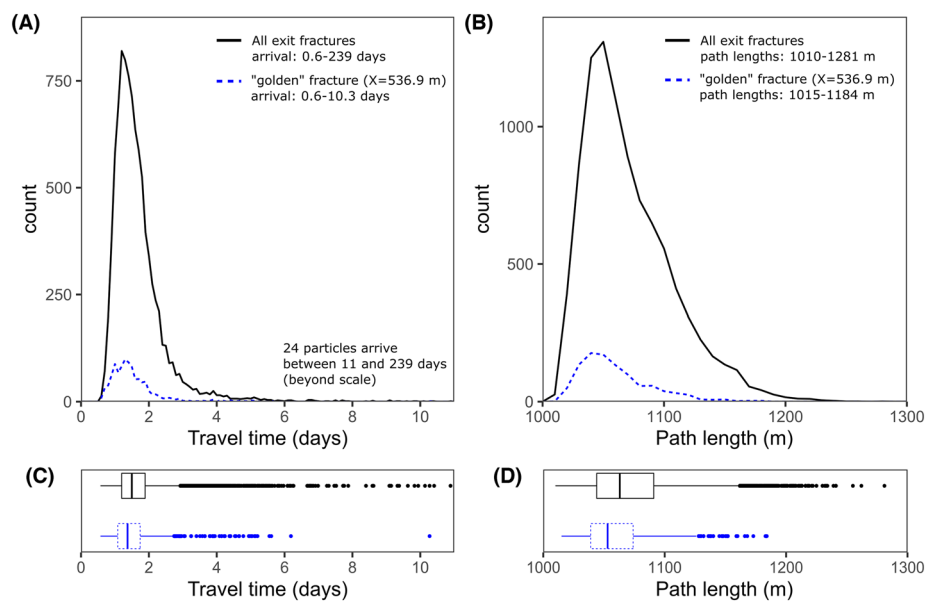


Fig. 9 Summary of tracing particle arrivals for all exit fractures and the “golden fracture” through which 10% of the 10,000 tracing particles exit. **A** Histogram of arrival time, i.e. synthetic tracer test result, truncated at 11 days for clarity (bin width = 0.1 day). **B** Histogram of path lengths (bin width of 10 m). **C** Boxplot of arrival times, truncated at 11 days. **D** Boxplot of path length

and 238.8 days, with 50% of particles arriving between 1.2 and 1.9 days (median 1.5 days) (Fig. 8A). Both the synthetic tracer return curve and the histogram of path length show a steep rise in arrival time with a long tail (Fig. 9A, B). The varied tracer particle arrival times are caused by the multiplicity of paths of varying lengths.

About 10% of tracer particles, including the first arrival, exit through a single fracture that we call here the “golden fracture”, located at $X = 536.9$ m. The pattern of arrival times and path lengths for this golden fracture are similar to those through all exit fractures (Fig. 9A, B). This suggests that the population of paths ending at the golden fracture is similar to that ending through other fractures.

Discussion

Applicability for reservoir engineering

The 2-D DFNs presented here constrain the permeabilities used in ECMs to model reservoir-scale processes in fracture-dominated geothermal reservoirs. Indeed, the average of pressure distributions from ensembles of 50 DFNs closely match ECMs with the same boundary conditions and distribution of rock types of varied fracture density. The vertical permeability for any geological unit in the ECM scales linearly with the fracture density in the backbone fracture network for that unit. Horizontal permeabilities are derived from the permeability anisotropy that naturally arises from the DFNs.

Based on the link between permeability and fracture density in the backbone networks for DFNs, ECMs can be populated with realistic permeabilities using PDFs derived for key fluid transport properties of the fracture networks. This

methodology could be applied on subdomains of any scale from single ECM model elements upward. Single element realisations of DFNs would show a level of variability not ordinarily represented with the ECMs. These ‘stochastic continuum models’ would allow realistic estimates of the variability of pressure distributions in fractured reservoirs without the computational cost of full 3-D DFN modelling. In addition, rapid interpretation of borehole images during a drilling campaign would provide the mean P_{10} , and hence, assuming that the fracture orientation is similar to that modelled in this paper, an indication of bulk mean flows and permeability anisotropy.

Hydrodynamic dispersion that is described by fluid particle tracing in the DFNs is a process which has not generally been accounted for in traditional continuum models of fluid and heat flow in geothermal systems. To represent fluid dispersion more generally in a continuum geothermal reservoir model, a hydrodynamic dispersion term (e.g. Schwartz and Smith 1988) must be added to the fluid and heat transport equations that are solved by the geothermal simulation code.

The synthetic tracer return curves arising from the DFN (Figs. 8, 9) are not exactly comparable to real tracer curves because dispersion along the fracture and tracer-rock interactions are not considered. Also, the situation represents tracers injected in a single borehole and sampled at distant producers intersecting fractures from the BBN. However, the steep rise and long tail of particle travel time across the domain resembles real tracer tests (e.g. Grant and Bixley 2011). We therefore propose that the fluid particle tracing briefly presented here could support improved interpretation of tracer tests through pervasively fractured geothermal reservoirs. In addition, the fluid tracing codes could be used to sample the natural flow across the reservoir as represented by an inflow from the entire lower boundary.

Choice of input fracture orientation and aperture

The results of DFNs presented here are applicable to pervasively fractured reservoirs where fractures have a dominant strike and are steeply dipping (dip magnitude $>60\text{--}70^\circ$). This fracture configuration is found throughout the TVZ, where borehole fracture orientations mirror those of the intensely faulted NE-SW-trending Taupo Rift (Villamor and Berryman 2001; Villamor et al. 2017). Similar fracture orientations occur in reservoirs such as the sandstone geothermal reservoirs of the Rhine Graben (Vidal and Genter 2018, and references therein).

Subordinate fracture orientations are observed in borehole images acquired in TVZ geothermal reservoirs and elsewhere (Massiot et al. 2017a; McNamara et al. 2019). Previous 2-D modelling has shown that adding such a subordinate fracture population with lower mean dip magnitude (60°) reduces the mean permeability anisotropy, but the change is slight and remains within the uncertainties (Kissling and Massiot 2019, 2021). Globally, volcanic geothermal systems commonly occur in fault interaction regions with several fracture orientations (Jolie et al. 2021). The results presented here could thus be applied in parts of these reservoirs that have one dominant fracture strike and high dip magnitude.

Hydraulic fracture aperture has a strong impact on permeability but is very difficult to estimate. Critically stressed fractures have an increased probability of being permeable because they are prone to be reactivated in shear mode and to have rough walls (Kissling et al. 2015; Jolie et al. 2016). Assigning a hydraulic fracture aperture based on the fracture's orientation with respect to a defined in-situ stress field could be implemented in the code. The models do not explore the effects that connections along fracture paths could be severed by precipitation of hydrothermal by pyrite, or to a limited extent iron oxide and clays. We speculate that the high level of connectivity of the models would have some, but limited effects on the reservoir-scale permeabilities. In reservoirs (or parts thereof) where precipitation of hydrothermal minerals that have low acoustic amplitude is preponderant, and additional random parameter could be added to the ' β ' aperture factor. For application to other locations, β could also be tuned to reflect any additional data such as fracture tortuosity that decreases fracture permeability (Heap and Kennedy 2016); or additional calibration from field data such as well tests or micro-seismicity during stimulation (Barton et al. 2013; Masri et al. 2015).

Steady-state simulations of flows in rough fractures using a local cubic law approximation to the Navier–Stokes equations (Brush and Thompson 2003) show the effective permeabilities can be smaller than those in plane-parallel fractures by many orders of magnitude (Kirkby et al. 2016; pers. comm.; Aghajannezhad et al. 2022). The simulations further suggest that the shear failure offsets of fracture walls correlate strongly with effective fracture permeability (Kirkby et al. 2016). In this paper the aperture factor β , calibrated by matching DFN simulations with bulk reservoir scale flows, allows realistic estimates of fracture hydraulic aperture which allow the cubic flow law to be used.

Effect of varying fractured density, hence rock types, on flows and permeability anisotropy

In the TVZ geothermal reservoirs hosted in volcanic rocks, the fracture densities measured in borehole images imply that flows are most likely above the percolation threshold. Substantial flows can occur through the fractured rock that typically lies between large faults. These fractures connected at reservoir scales can explain the occurrence of permeable zones away from mapped faults. In addition, models presented here that do not consider effects of the matrix are applicable to reservoirs (or parts thereof) of porosity < 10–12% dominated by micro-cracks, i.e. in the TVZ found in high-temperature reservoir where chlorite and other high-temperature hydrothermal minerals dominate over smectite and illite (see Sect. “[Fracture system characteristics and input into models](#)”).

Models show that bulk mean flows increase from sheet-like andesite to ignimbrite to rhyolite, matching the increased mean fracture density. Elevated permeability in rhyolites, and especially in their fractured and brecciated margins, has previously been identified in TVZ reservoirs (Rosenberg et al. 2009; Mroczek et al. 2016; Milicich et al. 2016). Permeability anisotropy of ca. 13 ± 3 resulting from the models are similar for sheet-like andesite, ignimbrite and rhyolite (scatter is 3 standard deviations). Another major rock type in TVZ reservoirs is the metamorphic greywacke basement. There, numerous fractures are observed in borehole images (Wallis et al. 2012) but the mean

fracture densities and effects of the varied origin of fractures and veins on their potential to be permeable remain to be assessed. Further work is needed to summarise fracture geometries in borehole images in other lithologies (e.g. other ignimbrites than those studied at Wairakei).

For $P_{10} < 0.5 \text{ m}^{-1}$, the mean permeability anisotropy decreases, but the scatter (standard deviation) increases to the point where, at $P_{10} = 0.3 \text{ m}^{-1}$, any value less than ~ 20 is possible. In these cases, the mean flows are low and vary considerably depending on the specific geometry of each backbone network. This low P_{10} could occur in other lithologies than those considered in this study, in the TVZ or elsewhere.

Mean fracture densities in volcanic geothermal reservoirs elsewhere in the world are broadly similar to those presented in this study. In the Muara Laboh, Rantau Dedap and Wayan Windu geothermal fields in Indonesia (Masri et al. 2015; Wallis et al. 2020), P_{10} was measured in resistivity images to be 2.4 m^{-1} in lavas; 2.1 m^{-1} in intrusive rocks and $0.6\text{--}1.7 \text{ m}^{-1}$ in pyroclastic rocks. Imaging in the same borehole by both resistivity and acoustic techniques shows that more numerous, thinner fractures are recorded in resistivity logs (Davatzes and Hickman 2009). At the Wairakei Geothermal Field, there were about 2.5 times more fractures in the resistivity image than in acoustic images (McNamara et al. 2019). This estimate is crude but reasonable because, although it arises from images in different boreholes, the boreholes were closely-spaced and intersected similar lithologies and faults. Using the factor 2.5, P_{10} in the Indonesian fields would lie in the range $0.3\text{--}0.9 \text{ m}^{-1}$ if they were measured using acoustic images, i.e. a similar range to this study of TVZ reservoir rocks.

By contrast, the sandstones of the Rhine Graben measured by acoustic images have P_{10} of $0.25\text{--}0.4 \text{ m}^{-1}$ (Genter et al. 1997; Vidal and Genter 2018). Higher densities ($P_{10} > 10 \text{ m}^{-1}$) occur in the granite reservoir, clustered in fractured hydrothermally altered zones and the top of the granite batholith, associated with sub-horizontal joints related to surface-stress-relaxation during the unroofing (Genter and Traineau 1996). The low P_{10} in borehole sections between faults in the Rhine Graben boreholes in sandstones corresponds to them being at or below the percolation threshold in our models. This is supported by permeability zones being constrained to discrete fault zones (Vidal and Genter 2018, and references therein). Those systems lacking pervasive fracturing require a different approach to populating a continuum model, such as deterministic modelling of permeable faults (Baillieux et al. 2014; Sausse et al. 2010).

Advantages and limitations of the presented modelling process

The DFNs presented here assumed steady state flows in fractures governed by the cubic flow law, in a 2-D $1 \text{ km} \times 1 \text{ km}$ ‘reservoir scale’ model domain. In addition, fluid properties are held constant and there is no thermal or hydraulic coupling to the rock matrix which hosts the fracture networks.

Using the $1 \text{ km} \times 1 \text{ km}$ model domain has advantages over previous modelling (Kissling and Massiot 2018, 2019) where a $0.35 \text{ km} \times 0.35 \text{ km}$ model domain was used. In these models, the number of continuous permeable paths (and therefore the flow) across the model domain was overestimated because the dimension of the model domain was only 3.5 times greater than the longest fractures. Here, the model domain is ten times

larger than the longest fractures. Boundary effects are expected to be smaller and the calculated flows more accurately reflect the prescribed fracture orientation and density.

The models do not consider the presence of pores in the matrix. This choice is supported by (1) the scale of investigation of flows where fractures are much longer (1–100 m) than pores (< 1 mm), and (2) the dominance of micro-cracks over pores at thin-section scale in the andesites and some of the ignimbrites (see Sect. “[Fracture system characteristics and input into models](#)”). The effect of matrix permeability on those fracture reservoirs could be explored using approaches such as the pore-network simulation (Joekar-Niasar et al. 2012), especially for modeling supercritical geothermal where the space between mineral grains are potential flow paths due to the low fluid viscosity (Liu et al. 2022). This approach could also represent the potential openings at fracture intersections, that are documented at fault-scale (Faulds and Hinz 2015), but only anecdotally in borehole images. Given the multiple factors that affect fracture’s geometry, the simple approach taken here allows for more computationally-efficient reservoir-scale modelling.

Assuming constant fluid properties is not realistic for any New Zealand geothermal system at 1 km length scales, but making this assumption is generally fit-for-purpose for geothermal reservoir engineering purposes. For example, the Theis ‘line source solution’ (e.g. Grant and Bixley 2011) is commonly used to determine geothermal reservoir transmissivity and storativity in interference tests, and is derived assuming fixed fluid properties and a simplified cylindrical geometry. As with the work described in this paper, assuming fixed fluid properties results in a linear equation for the pressure, and this framework will allow superposition of pressure solutions with (for example) multiple production boreholes, without the complications introduced by temperature-dependent fluid properties.

Assuming isothermal conditions also implies that no heat transfer occurs between the fluid in the fractures and the surrounding rock matrix. It is difficult to ascertain the effect of this assumption as it depends on many unknown factors. Some of these have been identified through simple numerical models of fractures in simplified geometries. For example, Zhou et al. (2022) have validated a simple analytic model of flow in a single fracture, and find that important parameters governing the heat transfer between fracture and matrix are the hydraulic fracture aperture and the thermal dispersivity in the fracture. In the context of a Hot Dry Rock (HDR) setting, Kolditz (1995) compares single- and multiple-fracture approximations including 1-D heat conduction orthogonal to the fracture(s) into the matrix, and finds reasonable (~ 10% level) agreement with 3-D numerical models, but again the geometry of the fracture networks is greatly simplified.

Sophisticated multi-physics packages designed for in-depth studies of fluid flow in 3-D fracture systems are required for developing EGS, where heat transfer between a small number of fractures and the surrounding matrix is of primary importance (Kennedy et al. 2021; Doe et al. 2022). The high density and pervasiveness of fractures in naturally fractured geothermal reservoirs, such as those in New Zealand, make them more amenable to the probabilistic approach to describing reservoir permeabilities outlined in this paper. Codes such as DFNWorks (Hyman et al. 2015) offer the capabilities to handle fluid flow and heat transfer between fractures and matrix in general 3-D fracture

networks, but this modelling is computationally expensive and could not provide statistical descriptions of reservoir properties for reservoir modelling and engineering purposes at 1 km scale as demonstrated in this paper.

The simple physics (Darcy flow in fractures, rectangular fractures, isothermal conditions, 2D models, averaged fracture geometries) used in this paper allow modelling at reservoir scale. The simple relationship between measured P_{10} and reservoir scale permeability, its anisotropy and its variability arising from modelling TVZ-like fracture networks at reservoir scale is aimed to provide rapid reasonable estimates as soon as borehole images are interpreted, for reservoir engineering purposes. In addition, YFLOW provides the capability to rapidly trace fluid particles through these systems to inform analysis of tracer tests.

Conclusions

Representing fracture networks in continuum models of fractured geothermal systems to model reservoir behaviour is challenging. This study provides geologically-realistic permeabilities that can be used to improve modelling of pervasively fractured TVZ reservoirs, in areas that occur between large permeable faults. The new DFN codes provide efficient 2-D fracture network generation and flow calculations at reservoir scale ($1 \text{ km} \times 1 \text{ km}$; ca. 500,000 fractures) with intensive parallel computing.

The fracture densities used in the models encompass three rock types common in TVZ geothermal reservoirs as measured on borehole images: sheet-like andesite, ignimbrite and small-volume rhyolite lavas and breccias. Results are applicable to fractured reservoirs (or part thereof) having a dominant fracture strike and steep dip magnitude ($>60\text{--}70^\circ$), as measured in borehole images in TVZ reservoirs.

PDFs of permeabilities are calculated from 1000 DFN realisations. Mean flows are linearly correlated to fracture densities down to the percolation threshold. Permeability anisotropy of $\text{ca. } 13 \pm 3$ arises from the DFN for fracture densities and orientations consistent with TVZ reservoirs. The multiplicity of connected paths at reservoir scale causes fluid dispersion in space and time. The synthetic tracer return curves resemble real tracer return curves, and demonstrate the importance of considering pervasive fracture networks in reservoir behaviour.

A probabilistic approach to populate ECM for reservoir engineering purposes using probability distributions arising from the DFNs is proposed. Permeabilities and permeability anisotropy in ECM can be populated by sampling from the PDF arising from multiple DFN realizations. At the $1 \text{ km} \times 1 \text{ km}$ scale, the average of pressure distributions in >50 DFN realisations approaches that in an ECM. A real reservoir at a given time may correspond to one of the DFN realisations.

Appendix 1

Figure 10 presents the flowchart of the XFRAC and YFLOW codes.

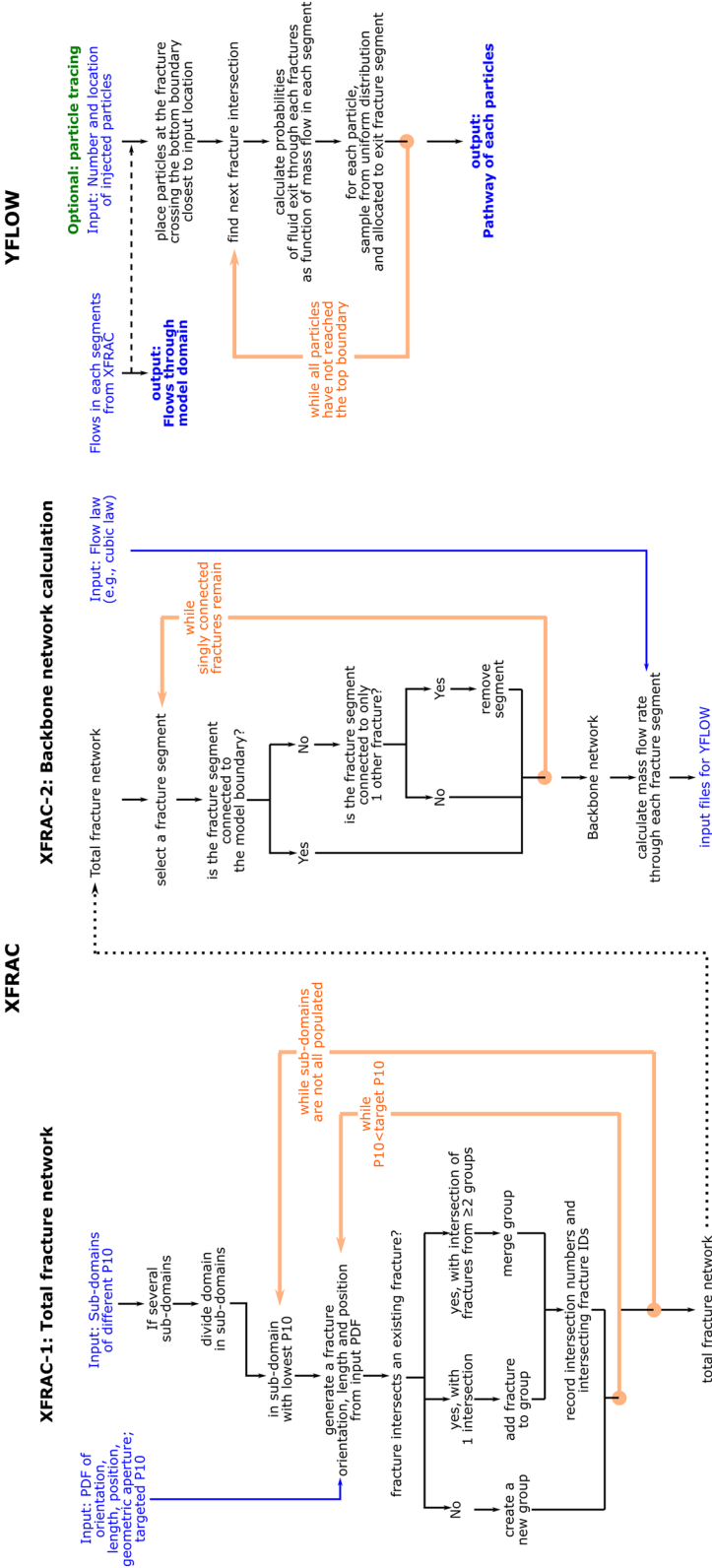


Fig. 10 Flowchart of codes

Appendix 2

Code validation examples

The codes XFRAC and YFLOW are validated here using a simple network with two orthogonal fractures by comparing the code's results to the analytical solution.

Firstly, we consider a single fracture with geometric aperture $h=0.1$ m and $\beta=0.002$ crossing the entire domain, parallel to the pressure gradient. The permeability of this fracture is:

$$k = (\beta h)^2 / 12 = 3.333 \times 10^{-9} \text{ m}^2 \quad (3)$$

From Darcy's law, the mass flux of water carried by this fracture is

$$Q = (k/\mu) \rho \Delta P / \Delta L \quad (4)$$

where $\Delta P / \Delta L$ is the pressure gradient applied along the fracture, ρ is the fluid density, and μ is the dynamic viscosity of the fluid. As with other models described in this paper, the pressure gradient $\Delta P / \Delta L = 1$ MPa/km or 10^3 Pa/m, $\rho = 692$ kg/m³, and $\mu = 8.74 \times 10^{-5}$ Pa.s. We find a mass flux of:

$$Q_o = 26.393 \text{ kg/m}^2/\text{s} \quad (5)$$

The total mass flow rate of fluid is then Q_o multiplied by the cross-sectional area of the fracture in the direction of flow, $H\beta h$, where H is 100 m:

$$V_o = 0.5279 \text{ kg/s} \quad (6)$$

Next, we consider a simple network of two fractures which intersect at right angles (Fig. 11). The network connects two boundaries—the lower boundary and one of the lateral boundaries. Case B represents the model where the fracture network in case A is rotated by 90°, in the same way that we use to calculate the permeability anisotropy of more realistic fracture networks in this paper.

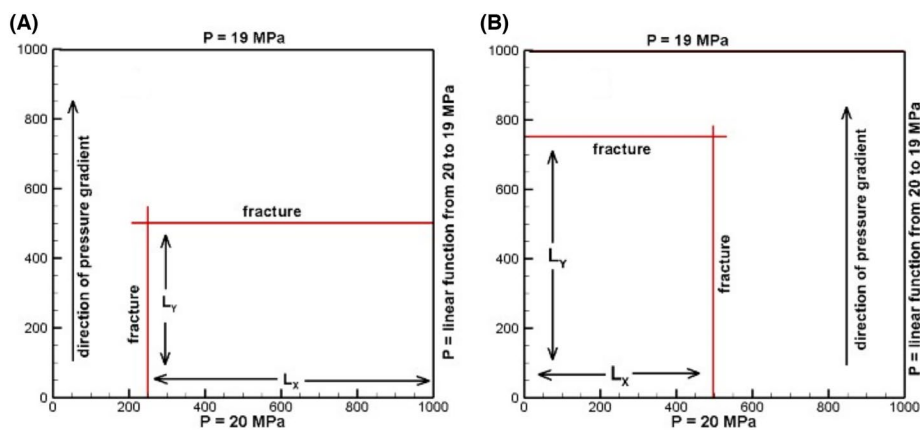


Fig. 11 Layout of a simple test problem. In both cases **A** and **B** the pressure gradient is parallel to the Y-axis but in case **B** the fracture network is rotated by 90° with respect to case **A**. This is analogous to the procedure used to calculate the permeability anisotropy in the paper

Table 5 Comparison of results from 2-fracture models run with XFRAC/YFLOW and analytical calculations (Eq. 7), for various combinations of fracture length

Model	L_X, L_Y	$L_Y/(L_X + L_Y)$	Mass flow (kg/s)		Pressure (MPa)	
			Model	Eq. 7	Model	Eq. 8
1 A	500, 500	0.5000	0.2639	0.2639	19.750	19.750
B	500, 500	0.5000	0.2639	0.2639	19.250	19.250
2 A	750, 500	0.4000	0.2111	0.2111	19.800	19.800
B	750, 500	0.6000	0.3167	0.3167	19.450	19.450
3 A	750, 750	0.5000	0.2639	0.2639	19.625	19.650
B	750, 750	0.5000	0.2639	0.2639	19.375	19.375
4 A	100, 300	0.7500	0.3959	0.3959	19.775	19.775
B	100, 300	0.2500	0.1320	0.1320	19.025	19.025

The flow through the network depends on the difference of the two boundary pressures that the network intersects and the length of the path connecting them to the model boundaries, $L_X + L_Y$ (as defined on Fig. 11). The boundary pressures are respectively 20 bar and $20 - 10^{-3} L_Y$ MPa, where 10^{-3} MPa/m (10^3 Pa/m) is the prescribed pressure gradient along either lateral boundary. The pressure difference driving the flow is therefore $10^{-3} L_Y$ MPa, and this occurs over a distance of $L_X + L_Y$. So, the flow rate in the fracture network is:

$$V = V_o L_Y / (L_X + L_Y) \quad (7)$$

where the mass flow rate V_o is calculated above based on a pressure gradient of 10^3 Pa/m.

In this model there is a single unknown pressure at the intersection of the two fractures. As the pressure gradient is constant through the fracture network, the pressure at the intersection is obtained using linear interpolation between the two boundary pressures:

$$P(\text{intersection}) = 20.0 - 1. L_Y / (L_X + L_Y) \text{ MPa} \quad (8)$$

The outputs of models using the codes XFRAC and YFLOW for four combinations of values of L_X and L_Y are consistent with predictions from Eqs. 7 and 8 (Table 5). Note that, as predicted, if $L_X = L_Y$ (as in models 1 and 3, Table 5), $V = V_o/2$ for all values of L_X and L_Y and that the mass flow rates for cases A and B for each model always sum to V_o .

Abbreviations

BBN	BackBone network
DFN	Discrete fracture network
ECM	Equivalent continuum model
EGS	Enhanced geothermal system
HDR	Hot dry rock (geothermal system)
MFD	Mean fracture direction
MINC	Multiple interacting continua
P_{10}	Fracture density measured along boreholes, real or virtual
TVZ	Taupō volcanic zone

Supplementary Information

The online version contains supplementary material available at <https://doi.org/10.1186/s40517-023-00262-6>.

Additional file 1: Figure S1. Probability density function of **A** total number of fractures normalized by domain area, **B** mean flow along pressure gradient normalized by domain length and **C** permeability anisotropy. Each sub-figure show results for domains of 1 km x 1 km and 0.5 km x 0.5 km. Model A ($P_{10} = 0.6$ m-1).

Additional file 2: Figure S2. Probability density function of **A** total number of fractures, **B** flow along pressure gradient and **C** permeability anisotropy using 1000 realisations (black thick line) versus 100 realisations (five coloured thin lines for each parameter). Model A (uniform, $P_{10} = 0.6$ m-1).

Additional file 3: Figure S3. Evaluation of normal distribution fits for model A ($P_{10} = 0.6$ m-1): **A** total number of fractures, **B** mean flow along pressure gradient, **C** permeability anisotropy. Top left: histogram against probability density function. Top Right: theoretical quantiles against empirical ones (Q–Q plot). Bottom left: empirical cumulative distribution against fitted distribution functions. Bottom right: theoretical probabilities against empirical ones.

Additional file 4: Figure S4. Poor normal distribution fits for total number of fractures, flow along pressure gradient and permeability anisotropy. The only cases that are not well fitted by a normal distribution are: **A** flow along pressure gradient for $P_{10} = 0.2$ m-1, **B** Permeability anisotropy for $P_{10} = 0.4$ m-1, **C** permeability anisotropy for $P_{10} = 0.3$ m-1, **D** Permeability anisotropy for $P_{10} = 0.2$ m-1 (very poor fit as only 5 values are defined). Same graphics as Figure S3.

Additional file 5: Figure S5. Goodness of fit of gaussians on total number of fractures, mean flow along pressure gradient and permeability anisotropy. **A** Skewness, **B** Kurtosis. Grey-dashed lines are at 0.

Additional file 6: Table S1. Summary statistics of model realisations for model size 0.5 km x 0.5 km (Additional file 1: Figure S1). Numbers reported as mean \pm 1 standard deviation. 1000 realisations per model. The permeability anisotropy in the final column is the ratio of the along flow to the across flow.

Additional file 7: Effects of number of realisations and domain size; and Assessment of distribution fitting.

Acknowledgements

The authors thank our colleagues Peter McGavin, Peter Johnson, Sarah Milicich, Alison Kirkby and John Burnell for useful discussions on many aspects of this paper, and to David D. McNamara and Susan Ellis for discussions that led to the development of this research.

Author contributions

WK and CM designed the study. WK developed the codes. CM summarised borehole image interpretation for model input parameters. WK and CM interpreted the data and wrote the manuscript. Both authors read and approved the final manuscript.

Funding

This project is funded by the New Zealand Ministry of Business, Innovation and Employment through the GNS Science-led research programme Empowering Geothermal Energy (contract C05X1706).

Availability of data and materials

The codes developed for this study, with a minimal set of instructions, are available upon direct request to the authors. When requesting the codes, please outline the intended use and outcomes, and supply details of your research group/affiliation. The authors are under no obligation to offer support, but request that this paper be cited in any published material where the codes, or other ideas in the paper are used.

Input data for input fracture geometries were derived from McNamara et al. (2015b), Massiot et al. (2017a) and McNamara et al. (2019).

Declarations

Competing interests

The authors declare that they have no competing interests.

Received: 27 November 2022 Accepted: 26 June 2023

Published online: 01 August 2023

References

- Addison SJ, Winick JA, Mountain BW, Siega FL. Rotokawa reservoir tracer test history. In Proceedings NZ Geothermal Workshop. 2015.
- Aghajannezhad P, Sellier M, Becker S. The effect of geometrical and topological changes on the fluid flow through large-scale discrete fracture networks. *J Por Media*. 2022. <https://doi.org/10.1615/JPorMedia.2022040127>.
- Alappat C, Basermann A, Bishop AR, Fehske H, Hager G, Schenk O, Thies J, Wellein G. A recursive algebraic coloring technique for hardware-efficient symmetric sparse matrix-vector multiplication. *ACM Trans Parallel Comput*. 2020;7(3):1–37. <https://doi.org/10.1145/3399732>.

- Baillieux P, Schill E, Abdelfettah Y, Dezayes C. Possible natural fluid pathways from gravity pseudo-tomography in the geothermal fields of Northern Alsace (Upper Rhine Graben). *Geotherm Energy*. 2014;2(1):1–4. <https://doi.org/10.1186/s40517-014-0016-y>.
- Barton CA, Zoback MD. Self-similar distribution and properties of macroscopic fractures at depth in crystalline rock in the Cajon Pass Scientific Drill Hole. *J Geophys Res Solid Earth*. 1992;97(B4):5181–200. <https://doi.org/10.1029/91JB01674>.
- Barton CA, Zoback MD, Moos D. Fluid flow along potentially active faults in crystalline rock. *Geology*. 1995;23(8):683–6. [https://doi.org/10.1130/0091-7613\(1995\)023%3c\\$0683:FFAPAF%3e\\$2.3.CO;2](https://doi.org/10.1130/0091-7613(1995)023%3c$0683:FFAPAF%3e$2.3.CO;2).
- Barton CA, Moos D, Hartley L, Baxter S, Foulquier L, Holl H, Hogarth R, Brisbane A. Geomechanically coupled simulation of flow in fractured reservoirs. In: Proc. 38th NZ Geothermal Workshop, SGP-TR-198. 2013.
- Baujard C, Genter A, Dalmis E, Maurer V, Hehn R, Rosillette R, Vidal J, Schmittbuhl J. Hydrothermal characterization of wells GRT-1 and GRT-2 in Rittershoffen, France: implications on the understanding of natural flow systems in the Rhine Graben. *Geothermics*. 2017;1(65):255–68. <https://doi.org/10.1016/j.geothermics.2016.11.001>.
- Berkowitz B. Characterizing flow and transport in fractured geological media: a review. *Adv Water Resour*. 2002;25(8–12):861–84. [https://doi.org/10.1016/S0309-1708\(02\)00042-8](https://doi.org/10.1016/S0309-1708(02)00042-8).
- Bollhöfer M, Eftekhari A, Scheidegger S, Schenk O. Large-scale sparse inverse covariance matrix estimation. *SIAM J Sci Comput*. 2019;41(1):A380–401. <https://doi.org/10.1137/17M1147615>.
- Bollhöfer M, Schenk O, Janalik R, Hamm S, Gullapalli K. State-of-the-art sparse direct solvers. In: Grama A, Sameh AH, editors. *Parallel algorithms in computational science and engineering*. Cham: Birkhäuser; 2020. p. 3–33. https://doi.org/10.1007/978-3-030-43736-7_1.
- Bolós X, Cifuentes G, Macías JL, Sosa-Ceballos G, García-Tenorio F, Albor M. Geophysical imaging of fluid circulation and its relation with the structural system of Cerritos Colorados geothermal field, La Primavera caldera (Mexico). *J Volcanol Geoth Res*. 2019;1(369):238–49. <https://doi.org/10.1016/j.jvolgeores.2018.11.015>.
- Bonnet E, Bour O, Odling NE, Davy P, Main I, Cowie P, Berkowitz B. Scaling of fracture systems in geological media. *Rev Geophys*. 2001;39(3):347–83. <https://doi.org/10.1029/1999RG000074>.
- Bour O, Davy P. Connectivity of random fault networks following a power law fault length distribution. *Water Resour Res*. 1997;33(7):1567–83. <https://doi.org/10.1029/96WR00433>.
- Boussinesq J. Mémoire sur l'influence des frottements dans les mouvements réguliers des fluides. *J Math Pures Appl*. 1868;13(2):377–424.
- Brathwaite RL, Cargill HJ, Christie AB, Swain A. Lithological and spatial controls on the distribution of quartz veins in andesite- and rhyolite-hosted epithermal Au–Ag deposits of the Hauraki Goldfield New Zealand. *Miner Deposita*. 2001;36(1):1–2. <https://doi.org/10.1007/s001260050282>.
- Brush DJ, Thomson NR. Fluid flow in synthetic rough-walled fractures: Navier-Stokes, Stokes, and local cubic law simulations. *Water Resour Res*. 2003. <https://doi.org/10.1029/2002WR001346>.
- Buscarlet E, Moon H, Wallis I, Quinao J. Reservoir tracer test at the Ngatamariki geothermal field. In: Proceedings 37th New Zealand Geothermal Workshop. Vol. 18. 2018. p. 20.
- Cant JL, Siratovich PA, Cole JW, Villeneuve MC, Kennedy BM. Matrix permeability of reservoir rocks, Ngatamariki geothermal field, Taupo volcanic zone, New Zealand. *Geothermal Energy*. 2018;6(1):1–28. <https://doi.org/10.1186/s40517-017-0088-6>.
- Davatzes NC, Hickman SH. Fractures, stress and fluid flow prior to stimulation of well 27-15, Desert Peak, Nevada, EGS Project. In: Thirty-Fourth Workshop on Geothermal Reservoir Engineering. 2009.
- Davatzes NC, Hickman SH. Stress, fracture, and fluid-flow analysis using acoustic and electrical image logs in hot fractured granites of the Coso geothermal field, California, USA. In: Poppelreiter M, Garcia-Carballido C, Kraaijveld M, editors. *Dipmeter and borehole image log technology*. Tulsa: AAPG Memoir 92; 2010. p. 259–93. <https://doi.org/10.1306/13181288M923134>.
- Dershowitz WS, Herda HH. Interpretation of fracture spacing and intensity. In the 33rd US Symposium on Rock Mechanics (USRMS) 1992. ARMA-92-0757. OnePetro. 1992.
- Dershowitz WS, Einstein HH. Characterizing rock joint geometry with joint system models. *Rock Mech Rock Eng*. 1988;21(1):21–51. <https://doi.org/10.1007/BF01019674>.
- Dezayes C, Genter A, Valley B. Structure of the low permeable naturally fractured geothermal reservoir at Soultz. *CR Geosci*. 2010;342(7–8):517–30. <https://doi.org/10.1016/j.crte.2009.10.002>.
- Doe, TW, Riahi, A, Fu, P, Damjanac, B, Sonnenthal, EL, Finnla, A, Kennedy, BM, Blankenship, D. Performance evaluation of engineered geothermal systems using discrete fracture network simulations. In: Proceedings, 47th Workshop on Geothermal Reservoir Engineering. 2022.
- Faulds J, Hinz N. Favorable tectonic and structural settings of geothermal systems in the Great Basin region, western USA: proxies for discovering blind geothermal systems. In: Proceedings World Geothermal Congress, Melbourne, Australia, 19–25 April 2015. Nevada Bureau of Mines and Geology, University of Nevada, Reno. 2015.
- Faulkner DR, Jackson CA, Lunn RJ, Schlische RW, Shipton ZK, Wibberley CA, Withjack MO. A review of recent developments concerning the structure, mechanics and fluid flow properties of fault zones. *J Struct Geol*. 2010;32(11):1557–75. <https://doi.org/10.1016/j.jsg.2010.06.009>.
- Genter A, Traineau H. Analysis of macroscopic fractures in the HDR geothermal well EPS-1, Soultz-sous-Forêts, France. *J Volcanol Geoth Res*. 1996;72:121–41. [https://doi.org/10.1016/0377-0273\(95\)00070-4](https://doi.org/10.1016/0377-0273(95)00070-4).
- Genter A, Castaing C, Dezayes C, Tenzer H, Traineau H, Villemin T. Comparative analysis of direct (core) and indirect (borehole imaging tools) collection of fracture data in the Hot Dry Rock Soultz reservoir (France). *J Geophys Res Solid Earth*. 1997;102(B7):15419–31. <https://doi.org/10.1029/97JB00626>.
- Gillespie PA, Howard CB, Walsh JJ, Watterson J. Measurement and characterisation of spatial distributions of fractures. *Tectonophysics*. 1993;226(1–4):113–41. [https://doi.org/10.1016/0040-1951\(93\)90114-Y](https://doi.org/10.1016/0040-1951(93)90114-Y).
- Glaas C, Vidal J, Genter A. Structural characterization of naturally fractured geothermal reservoirs in the central Upper Rhine Graben. *J Struct Geol*. 2021;148:104370. <https://doi.org/10.1016/j.jsg.2021.104370>.

- Grant MA, Bixley PF. Geothermal reservoir engineering. 2nd ed. Burlington: Academic Press; 2011.
- Griffiths L, Heap MJ, Wang F, Daval D, Gilg HA, Baud P, Schmittbuhl J, Genter A. Geothermal implications for fracture-filling hydrothermal precipitation. *Geothermics*. 2016;64:235–45. <https://doi.org/10.1016/j.geothermics.2016.06.006>.
- Gudmundsson A. Fracture dimensions, displacements and fluid transport. *J Struct Geol*. 2000;22(9):1221–31. [https://doi.org/10.1016/S0191-8141\(00\)00052-3](https://doi.org/10.1016/S0191-8141(00)00052-3).
- Halwa L, Wallis IC, Lozada GT. Geological analysis of the volcanic subsurface using borehole resistivity images in the Ngatamariki Geothermal Field, New Zealand. In: 35th New Zealand Geothermal Workshop Proceedings, Rotorua 2013.
- Heap MJ, Kennedy BM. Exploring the scale-dependent permeability of fractured andesite. *Earth Planet Sci Lett*. 2016;447:956–63. <https://doi.org/10.1017/CBO9781107415324.004>.
- Hyman JD, Karra S, Makedonska N, Gable CW, Painter SL, Viswanathan HS. dfnWorks: a discrete fracture network framework for modeling subsurface flow and transport. *Comput Geosci*. 2015;1(84):10–9. <https://doi.org/10.1016/j.cageo.2015.08.001>.
- Intani RG, Golla GU, Syaffitri Y, Paramitasari HM, Nordquist GA, Nelson C, Giri GK, Sugandhi A. Improving the conceptual understanding of the Darajat geothermal field. *Geothermics*. 2020;83:101716. <https://doi.org/10.1016/j.geothermics.2019.101716>.
- Joekar-Niasar V, Hassanizadeh SM. Analysis of fundamentals of two-phase flow in porous media using dynamic pore-network models: a review. *Crit Rev Environ Sci Technol*. 2012;42(18):1895–976. <https://doi.org/10.1080/10643389.2011.574101>.
- Jolie E, Klinkmueller M, Moeck I, Bruhn D. Linking gas fluxes at Earth's surface with fracture zones in an active geothermal field. *Geology*. 2016;44(3):187–90. <https://doi.org/10.1130/G37412.1>.
- Jolie E, Scott S, Faulds J, Chambefort I, Axelsson G, Gutiérrez-Negrín LC, Regenspurg S, Ziegler M, Richter A, Zemedkun MT. Geological controls on geothermal resources for power generation. *Nat Rev Earth Environ*. 2021;2(5):324–39. <https://doi.org/10.1038/s43017-021-00154-y>.
- Kennedy, B, Blankenship, D, Doe, T, Riahi, A, Damjanac, B, Finnilla, A, et al. Performance evaluation of engineered geothermal systems using discrete fracture network simulations. In: Performance Evaluation of Engineered Geothermal Systems Using Discrete Fracture Network Simulations. Lawrence Berkeley National Laboratory. Report #: LBNL-2001392. 2021. <https://escholarship.org/uc/item/4168d73x>. Accessed 12 Jul 2023.
- Kirkby A, Heinson G, Krieger L. Relating permeability and electrical resistivity in fractures using random resistor network models. *J Geophys Res Solid Earth*. 2016;121(3):1546–64. <https://doi.org/10.1002/2015JB012541>.
- Kissling WM, Massiot C. Geometrical modelling of fracture networks in an andesite-hosted geothermal reservoir. In: Proceedings 39th New Zealand Geothermal Workshop 2017. 2017.
- Kissling WM, Massiot C. Modelling flows in discrete fracture networks derived from a New Zealand lava-hosted geothermal system. In: Proceedings 40th New Zealand Geothermal Workshop 2018. 2018.
- Kissling WM, Massiot C. Characteristics of flows in pervasively fractured andesites, Rotokawa geothermal field, New Zealand. In: Proceedings 41st New Zealand Geothermal Workshop 2019. 2019.
- Kissling WM, Massiot C. Permeability anisotropy and fluid dispersion pervasively fractured lavas, Rotokawa geothermal system, New Zealand. In: Proceedings World Geothermal Congress 2020+1. 2020.
- Kissling WM, Ellis SE, McNamara DD., Massiot, C. Modelling fluid flow through fractured rock: Examples using TVZ geothermal reservoirs. In: Proceedings 37th New Zealand Geothermal Workshop 2015. New Zealand Geothermal Workshop. 2015.
- Kissling WM. A testbed for a new-generation geothermal simulator. In: Proceedings 36th New Zealand Geothermal Workshop 2014. 2014.
- Kolditz O. Modelling flow and heat transfer in fractured rocks: dimensional effect of matrix heat diffusion. *Geothermics*. 1995;24(3):421–37. [https://doi.org/10.1016/0375-6505\(95\)00018-L](https://doi.org/10.1016/0375-6505(95)00018-L).
- Lang PS, Paluszny A, Zimmerman RW. Permeability tensor of three-dimensional fractured porous rock and a comparison to trace map predictions. *J Geophys Res Solid Earth*. 2014;119(8):6288–307. <https://doi.org/10.1002/2014JB011027>.
- Lee CC, Lee CH, Yeh HF, Lin HI. Modeling spatial fracture intensity as a control on flow in fractured rock. *Environ Earth Sci*. 2011;63(6):1199–211. <https://doi.org/10.1007/s12665-010-0794-x>.
- Lei Q, Latham JP, Tsang CF. The use of discrete fracture networks for modelling coupled geomechanical and hydrological behaviour of fractured rocks. *Comput Geotech*. 2017;1(85):151–76. <https://doi.org/10.1016/j.compgeo.2016.12.024>.
- Liotta D, Brogi A, Árnadóttir S, Ágústsson K, Thorsteinsdóttir U. Field evidence of the interplay between rift and transform structures in the Krafla geothermal area, N-Iceland. *Geothermics*. 2021;91:102039. <https://doi.org/10.1016/j.geothermics.2020.102039>.
- Liu R, Li B, Jiang Y, Huang N. Review: mathematical expressions for estimating equivalent permeability of rock fracture networks. *Hydrogeol J*. 2016;24(7):1623–49. <https://doi.org/10.1007/s10040-016-1441-8>.
- Liu B, Suzuki A, Watanabe N, Ishibashi T, Sakaguchi K, Ito T. Fracturing of granite rock with supercritical water for superhot geothermal resources. *Renewable Energy*. 2022;184:56–67. <https://doi.org/10.1016/j.renene.2021.11.062>.
- Ma Y, Gan Q, Zhang Y, Zhou L. Numerical simulation of the heat production potential of Guide Basin in China considering the heterogeneity and anisotropy of the reservoir. *Geothermics*. 2022;105:102508. <https://doi.org/10.1016/j.geothermics.2022.102508>.
- Maffucci R, Bigi S, Corrado S, Chiodi A, Di Paolo L, Giordano G, Invernizzi C. Quality assessment of reservoirs by means of outcrop data and “discrete fracture network” models: the case history of Rosario de La Frontera (NW Argentina) geothermal system. *Tectonophysics*. 2015;19(647):112–31. <https://doi.org/10.1016/j.tecto.2015.02.016>.
- Masri A, Barton C, Hartley L, Ramadhan Y. Structural permeability assessment using geological structural model integrated with 3D geomechanical study and discrete fracture network model in Wayang Windu Geothermal Field, West Java, Indonesia. In: Proceedings 40th Workshop of Geothermal Reservoir Engineering, Stanford, California 2015. 2015.

- Massiot C, Nicol A, McNamara DD, Townend J. Evidence for tectonic, lithologic, and thermal controls on fracture system geometries in an andesitic high-temperature geothermal field. *J Geophys Res Solid Earth*. 2017a;122(8):6853–74. <https://doi.org/10.1002/2017JB014121>.
- Massiot C, Townend J, Nicol A, McNamara DD. Statistical methods of fracture characterization using acoustic borehole televiewer log interpretation. *J Geophys Res Solid Earth*. 2017c;122(8):6836–52. <https://doi.org/10.1002/2017JB014115>.
- Massiot C, McLean K, McNamara DD, Sepúlveda F, Milicich SD. Discussion between a reservoir engineer and a geologist: permeability identification from completion test data and borehole image logs integration. In: New Zealand Geothermal Workshop 2017b Nov 22. 39th New Zealand Geothermal Workshop. 2017b.
- McNabb A, Dickinson G. Pressures in the Wairakei Geothermal Field (NZ) in its natural state. In: Proceedings 17th New Zealand Geothermal Workshop. 1995.
- McNamara DD, Massiot C, Lewis B, Wallis IC. Heterogeneity of structure and stress in the Rotokawa geothermal field, New Zealand. *J Geophys Res Solid Earth*. 2015;120(2):1243–62. <https://doi.org/10.1002/2014JB011480>.
- McNamara DD, Sewell S, Buscarlet E, Wallis IC. A review of the Rotokawa geothermal field, New Zealand. *Geothermics*. 2016;1(59):281–93. <https://doi.org/10.1016/j.geothermics.2015.07.007>.
- McNamara DD, Lister A, Prior DJ. Calcite sealing in a fractured geothermal reservoir: Insights from combined EBSD and chemistry mapping. *J Volcanol Geoth Res*. 2016;323:38–52. <https://doi.org/10.1016/j.jvolgeores.2016.04.042>.
- McNamara DD, Milicich SD, Massiot C, Villamor P, McLean K, Sepúlveda F, Ries WF. Tectonic controls on Taupo Volcanic Zone geothermal expression: insights from Te Mihi Wairakei Geothermal field. *Tectonics*. 2019;38(8):3011–33. <https://doi.org/10.1029/2018TC005296>.
- Milicich SD, Clark JP, Wong C, Askari M. A review of the Kawerau geothermal field, New Zealand. *Geothermics*. 2016;1(59):252–65. <https://doi.org/10.1016/j.geothermics.2015.06.012>.
- Milicich SD, Chambeffort I, Wilson CJ, Alcaraz S, Ireland TR, Bardsley C, Simpson MP. A zircon U-Pb geochronology for the Rotokawa geothermal system, New Zealand, with implications for Taupō Volcanic Zone evolution. *J Volcanol Geotherm Res*. 2020;389:106729. <https://doi.org/10.1016/j.jvolgeores.2019.127065>.
- Milloy SF, Mclean K, McNamara DD. Comparing borehole televiewer logs with continuous core: an example from New Zealand. In: World Geothermal Congress Proceedings. 2015.
- Mroczek EK, Milicich SD, Bixley PF, Sepúlveda F, Bertrand EA, Soengkono S, Rae AJ. Ohaaki geothermal system: refinement of a conceptual reservoir model. *Geothermics*. 2016;1(59):311–24. <https://doi.org/10.1016/j.geothermics.2015.09.002>.
- Mutonga, M, Yasuhiro F. An insight of the subsurface through borehole images—case study of MW-34 Menengai geothermal field, Kenya. In: Proceedings 43rd New Zealand Geothermal Workshop. 2021.
- Neuman SP. Trends, prospects and challenges in quantifying flow and transport through fractured rocks. *Hydrogeol J*. 2005;13(1):124–47. <https://doi.org/10.1007/s10040-004-0397-2>.
- Norini G, Carrasco-Núñez G, Corbo-Camargo F, Lermo J, Rojas JH, Castro C, Bonini M, Montanari D, Corti G, Moratti G, Piccardi L. The structural architecture of the Los Hornos volcanic complex and geothermal field. *J Volcanol Geoth Res*. 2019;1(381):312–29. <https://doi.org/10.1016/j.jvolgeores.2019.06.010>.
- O'Sullivan MJ, Renaud T, Gravatt MJ, Riffault J, Popineau J, O'Sullivan JP, Ruiz NC, Sophy M. An updated numerical model of the Ohaaki Geothermal Field. Vol. 23. In: Proceedings 43rd New Zealand Geothermal Workshop 2021. p. 25.
- Priest SD. Determination of discontinuity size distributions from scanline data. *Rock Mech Rock Eng*. 2004;37(5):347–68. <https://doi.org/10.1007/s00603-004-0035-2>.
- Pruess K. TOUGH2-A general-purpose numerical simulator for multiphase fluid and heat flow. Lawrence Berkeley National Laboratory. LBNL Report #: LBL-29400. 1991. <https://escholarship.org/uc/item/0wx8q119>. Accessed 12 Jul 2023.
- Pruess K. Brief guide to the MINC-method for modeling flow and transport in fractured media. CA (United States): Lawrence Berkeley Lab., LBNL Report #: Lbl-32195. 1992. <https://www.osti.gov/servlets/purl/6951290-15RBBn/>. Accessed 12 Jul 2023.
- Ramadhan Y, Masri, A. Fracture characterization through image log analysis in Wayang Windu geothermal. In: Proceedings Indonesia International Geothermal Convention & Exhibition. 2014.
- Romano V, Bigi S, Carnevale F, Hyman JD, Karra S, Valocchi AJ, Tartarello MC, Battaglia M. Hydraulic characterization of a fault zone from fracture distribution. *J Struct Geol*. 2020;135:104036. <https://doi.org/10.1016/j.jsg.2020.104036>.
- Rosenberg MD, Bignall G, Rae AJ. The geological framework of the Wairakei-Tauhara geothermal system, New Zealand. *Geothermics*. 2009;38(1):72–84. <https://doi.org/10.1016/j.geothermics.2009.01.001>.
- Sausse J, Dezayes C, Dorbath L, Genter A, Place J. 3D model of fracture zones at Soultz-sous-Forêts based on geological data, image logs, induced microseismicity and vertical seismic profiles. *CR Geosci*. 2010;342(7–8):531–45. <https://doi.org/10.1016/j.crte.2010.01.011>.
- Schenk O, Gärtner, K. Pardiso user guide version 7.2 (updated December 28, 2020).
- Schwartz FW, Smith L. A continuum approach for modeling mass transport in fractured media. *Water Resour Res*. 1988;24(8):1360–72.
- Sepúlveda F, Rosenberg MD, Rowland JV, Simmons SF. Kriging predictions of drill-hole stratigraphy and temperature data from the Wairakei geothermal field, New Zealand: implications for conceptual modeling. *Geothermics*. 2012;1(42):13–31. <https://doi.org/10.1016/j.geothermics.2012.01.002>.
- Sieh K, Natawidjaja D. Neotectonics of the Sumatran fault, Indonesia. *J Geophys Res Solid Earth*. 2000;105(B12):28295–326. <https://doi.org/10.1029/2000JB900120>.
- Siratovich PA, Heap MJ, Villeneuve MC, Cole JW, Reuschlé T. Physical property relationships of the Rotokawa Andesite, a significant geothermal reservoir rock in the Taupo Volcanic Zone, New Zealand. *Geotherm Energy*. 2014;2(1):1–31. <https://doi.org/10.1186/s40517-014-0010-4>.
- Stimar J, Nordquist G, Suminar A, Sirad-Azwar L. An overview of the Awibengkok geothermal system, Indonesia. *Geothermics*. 2008;37(3):300–31. <https://doi.org/10.1016/j.geothermics.2008.04.004>.

- Stimac J, Sihotang AM, Mussofan W, Baroek M, Jones C, Moore JN, Schmitt AK. Geologic controls on the Muara Laboh geothermal system, Sumatra, Indonesia. *Geothermics*. 2019;1(82):97–120. <https://doi.org/10.1016/j.geothermics.2019.06.002>.
- Torabi A, Berg SS. Scaling of fault attributes: a review. *Mar Pet Geol*. 2011;28(8):1444–60. <https://doi.org/10.1016/j.marpetgeo.2011.04.003>.
- Vidal J, Genter A. Overview of naturally permeable fractured reservoirs in the central and southern Upper Rhine Graben: insights from geothermal wells. *Geothermics*. 2018;1(74):57–73. <https://doi.org/10.1016/j.geothermics.2018.02.003>.
- Vidal J, Genter A, Schmittbuhl J. Pre- and post-stimulation characterization of geothermal well GRT-1, Rittershoffen, France: insights from acoustic image logs of hard fractured rock. *Geophys J Int*. 2016;206(2):845–60. <https://doi.org/10.1093/gji/ggw181>.
- Villamor P, Berryman K. A late Quaternary extension rate in the Taupo Volcanic Zone, New Zealand, derived from fault slip data. *NZ J Geol Geophys*. 2001;44(2):243–69. <https://doi.org/10.1080/00288306.2001.9514937>.
- Villamor P, Berryman KR, Ellis SM, Schreurs G, Wallace LM, Leonard GS, Langridge RM, Ries WF. Rapid evolution of subduction-related continental intraarc rifts: the Taupo Rift, New Zealand. *Tectonics*. 2017;36(10):2250–72. <https://doi.org/10.1002/2017TC004715>.
- Wallis IC, McNamara D, Rowland JV, Massiot C. The nature of fracture permeability in the basement greywacke at Kawerau Geothermal Field, New Zealand. In: *Proceedings, Thirty-Seventh Workshop on Geothermal Reservoir Engineering*. Stanford University Stanford, CA. 2012. p. 1–9.
- Wallis I, Rowland J, Dempsey D, Allan G, Sidik R, Martikno R, McLean K, Sihotang M, Azis H, Baroek M. Approaches to imaging Feedzone diversity with case studies from Sumatra, Indonesia and the Taupo Volcanic Zone, New Zealand. Vol 24. In: *Proceedings 42nd New Zealand Geothermal Workshop*. 2020. p. 26.
- Winick J, Siega F, Addison S, Richardson I, Mountain B, Barry B. Coupled iodine-125 and 2NSA reservoir tracer testing at the Rotokawa Geothermal Field, New Zealand. In: *Proceedings World Geothermal Congress*. 2015.
- Wooding RA. Large-scale geothermal field parameters and convection theory. *NZ J Sci*. 1978;21.
- Wyering LD, Villeneuve MC, Wallis IC, Siratovich PA, Kennedy BM, Gravley DM, Cant JL. Mechanical and physical properties of hydrothermally altered rocks, Taupo Volcanic Zone, New Zealand. *J Volcanol Geoth Res*. 2014;1(288):76–93. <https://doi.org/10.1016/j.jvolgeores.2014.10.008>.
- Zhao Z, Jing L, Neretnieks I. Evaluation of hydrodynamic dispersion parameters in fractured rocks. *J Rock Mech Geotech Eng*. 2010;2(3):243–54. <https://doi.org/10.3724/SPJ.1235.2010.00243>.
- Zhou D, Tatmir A, Niemi A, Tsang CF, Sauter M. Study on the influence of randomly distributed fracture aperture in a fracture network on heat production from an enhanced geothermal system (EGS). *Energy*. 2022;250:123781. <https://doi.org/10.1016/j.energy.2022.123781>.
- Ziegler M, Rajabi M, Heidbach O, Hersir GP, Ágústsson K, Árnadóttir S, Zang A. The stress pattern of Iceland. *Tectonophysics*. 2016;2(674):101–13. <https://doi.org/10.1016/j.tecto.2016.02.008>.
- Zimmerman RW, Bodvarsson GS. Hydraulic conductivity of rock fractures. *Transp Porous Media*. 1996;23(1):1–30. <https://doi.org/10.1007/BF00145263>.

Publisher's Note

Springer Nature remains neutral with regard to jurisdictional claims in published maps and institutional affiliations.

Submit your manuscript to a SpringerOpen[®] journal and benefit from:

- Convenient online submission
- Rigorous peer review
- Open access: articles freely available online
- High visibility within the field
- Retaining the copyright to your article

Submit your next manuscript at ► [springeropen.com](https://www.springeropen.com)